Department of Materials Science and Engineering

Numerical Modeling of Dehydrogenation and Denitrogenation in Industrial Vacuum Tank Degassers

Shan Yu

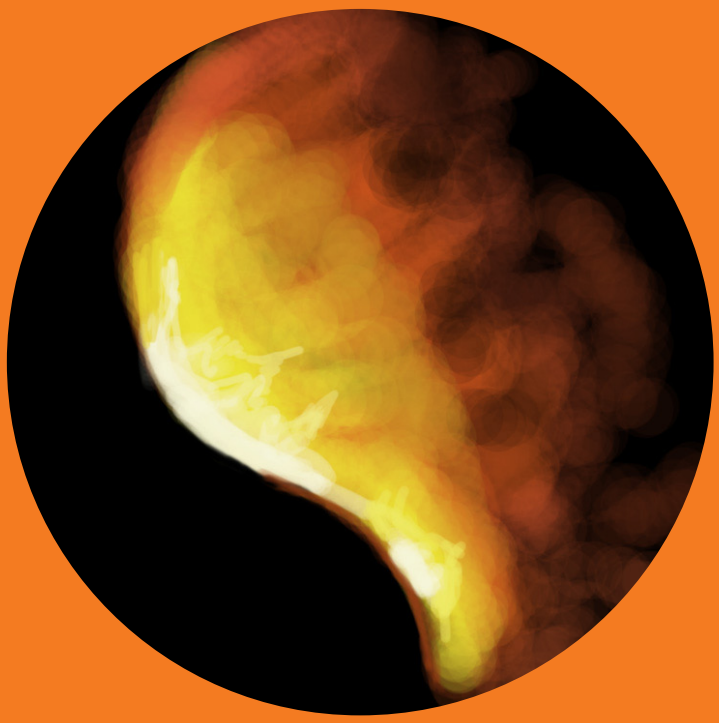

Aalto University

DOCTORAL DISSERTATIONS

Aalto University publication series
DOCTORAL DISSERTATIONS 131/2014

Numerical Modeling of Dehydrogenation and Denitrogenation in Industrial Vacuum Tank Degassers

Shan Yu

A doctoral dissertation completed for the degree of Doctor of Science (Technology) to be defended, with the permission of the Aalto University School of Chemical Technology, at a public examination held at the lecture hall V1 of the school (Espoo, Finland) on 3 October, 2014, at 12 noon.

Aalto University
School of Chemical Technology
Department of Materials Science and Engineering
Metallurgy

Supervising professor
Professor Seppo Louhenkilpi

Thesis advisor
Professor Seppo Louhenkilpi

Preliminary examiners
Professor Timo Fabritius, University of Oulu, Finland
Professor Pär Jönsson, KTH Royal Institute of Technology, Sweden

Opponent
Professor Henrik Saxén, Åbo Akademi University, Finland

Aalto University publication series
DOCTORAL DISSERTATIONS 131/2014

ISBN 978-952-60-5838-2
ISBN 978-952-60-5839-9 (pdf)
ISSN-L 1799-4934
ISSN 1799-4934 (printed)
ISSN 1799-4942 (pdf)
http://urn.fi/URN:ISBN:978-952-60-5839-9

Images: "Tapping" (cover)

Unigrafia Oy
Helsinki 2014

Finland

441 697
Printed matter

Aalto University

Abstract

Aalto University, P.O. Box 11000, FI-00076 Aalto www.aalto.fi

Author
Shan Yu

Name of the doctoral dissertation
Numerical Modeling of Dehydrogenation and Denitrogenation in Industrial Vacuum Tank Degassers

Publisher School of Chemical Technology

Unit Department of Materials Science and Engineering

Series Aalto University publication series DOCTORAL DISSERTATIONS 131/2014

Field of research Metallurgy

Manuscript submitted 2 June 2014 **Date of the defence** 3 October 2014

Permission to publish granted (date) 26 August 2014 **Language** English

☐ **Monograph** ☒ **Article dissertation (summary + original articles)**

Abstract

Hydrogen and nitrogen are inescapable elements in all commercial steel products and the presence of dissolved hydrogen and nitrogen in liquid steel can cause various problems in most of the final products. In general, the reduction of these elements in liquid steel is required in most steelmaking companies, where vacuum treatment is typically applied to remove these impurities.

The main focus of this thesis work has been put on investigating the dehydrogenation and/or denitrogenation behavior in a number of operational vacuum tank degassers (VTD) from different industrial plants. A literature review on various investigations and modeling techniques in the related field was firstly presented in this report. Based on the developed theories and methods that are relatively separate in the open literature, an integrated computational fluid dynamics (CFD) model was built to better understand the degassing process on an industrial scale and more importantly, for accurate predictions that are of considerable importance to industrial process operators.

The CFD model consists of two sub-routines for calculating multiphase flows and species transportations, respectively. The commercial CFD package of ANSYS FLUENT was adopted and augmented by various user-defined functions. As for the multiphase sub-model, the standard *k-epsilon* equations were extended by adding extra source terms to consider the impact of gas injections on turbulence quantities. The sub-model was validated by using literature data for an aqueous system whose similarity represented one of the industrial VTDs studied in this work. With the extended *k-epsilon* equations, deviations from measured data of axial liquid velocity and turbulent kinetic energy were lower than 13 % and 18 % respectively, whereas the deviations were about 30 % and 85 % with the standard equations. For mass transfer calculations, two fundamental expressions that have been commonly employed to compute mass transfer coefficient in gas-liquid systems were assessed. Comparisons with process data showed that the eddy-cell correlation provides a better prediction under the studied conditions. The versatility of the CFD model was further demonstrated by performing extensive simulations to cover the effect of gas flow rate, initial element (i.e., hydrogen and nitrogen) content and steel compositions on final element content and degassing rate. For hydrogen removal, deviations from measured data in different industrial plants were ranged between 6 % and 14 % and for nitrogen removal, the deviations were generally lower than 13 %.

Keywords CFD, Dehydrogenation, Denitrogenation, Vacuum tank degasser

ISBN (printed) 978-952-60-5838-2 **ISBN (pdf)** 978-952-60-5839-9

ISSN-L 1799-4934 **ISSN (printed)** 1799-4934 **ISSN (pdf)** 1799-4942

Location of publisher Helsinki **Location of printing** Helsinki **Year** 2014

Pages 127 **urn** http://urn.fi/URN:ISBN:978-952-60-5839-9

Preface

The work presented in this thesis was carried out at the Metallurgy Research Group of Aalto University (AU) during the years between 10.2009 and 2.2014. I here gratefully acknowledge the financial support from CSC (the China Scholarship Council), TEKES (the Finnish Funding Agency for Technology and Innovation), the ELEMET Program of FIMECC (the Finnish Metals and Engineering Competence Cluster) as well as RFCS (the Research Fund for Coal and Steel, RFCS-CT-2009-00030: HYDRAS).

I would like to express my deepest gratitude to my supervisor Prof. Seppo Louhenkilpi for his excellent guidance. Thank you for always believing in and constantly encouraging me during the course of this work.

My special thanks go to Prof. Lauri Holappa (with AU) and Prof. Zongshu Zou with Northeastern University of China (NEU), for their big roles in paving the road to studying in Finland for me. I am also thankful to Prof. Nan Wang (with NEU) for her outstanding supervision during my master thesis work and her moral support during my applying to study abroad. I am grateful to Jyrki Miettinen and Pilvi Oksman for being my co-authors, and to Benjamin Wilson for language corrections of the final draft. I thank Heli for being a partner, companion, and listener since the very first day I arrived in Finland. I thank Lea, Merja, Leena, Harri and Leif for helping me in countless technical and office-related issues. My colleagues and friends in the research group MTG and TDM, certainly deserve my profound appreciation for their generous help in many ways.

I highly acknowledge my industrial partners from different projects I have been luckily involved in during the past years. Stefano Baragiola from RIVA (Italy), Axel Sormann from Voestalpine Stahl (Austria), Seppo Ollila and Tuomas Antola from Ruukki Metals (Finland), Borja Peña Quintero from Tecnalia (Spain), Iñigo Unamuno from Gerdau (Spain), Gian Franco Lovicu from University of Pisa (Italy) and John Niska from Swerea Mefos (Sweden), thank you for providing me industrial measurements and all the invaluable discussions.

I am grateful to First Secretaries Zong Gang (former) and Deng Liming with the Education Section of Chinese Embassy in Finland for dealing with all issues related to the fund provided by CSC. I also owe a big thank you to my Chinese friends around me in this land. Thank you guys, for all the good times we have spent together.

I thank my parents and parents-in-law for their understanding and everlasting love. This will be incomplete if I don't mention my dearly beloved husband and son. Lei, thank you for your indispensable companion over the years and for giving me the best in life and Ruike, you are always the biggest support to me and daddy when we are down.

Espoo, August 1st, 2014

Shan Yu

List of Publications

The present report is mainly based on the following papers:

I. **Shan Yu** and Seppo Louhenkilpi: Numerical Simulation of Dehydrogenation of Liquid Steel in the Vacuum Tank Degasser, *Metallurgical and Materials Transactions B*, 44 (2013), pp. 459-468.

II. **Shan Yu**, Jyrki Miettinen and Seppo Louhenkilpi: Numerical Study on the Removal of Hydrogen and Nitrogen from the Melt of Medium Carbon Steel in Vacuum Tank Degasser, *Materials Science Forum*, 762 (2013), pp. 253-260.

III. **Shan Yu**, Jyrki Miettinen and Seppo Louhenkilpi: Modeling Study of Nitrogen Removal from the Vacuum Tank Degasser, *Steel Research International*, DOI: 10.1002/srin.201300262.

IV. **Shan Yu**, Jyrki Miettinen, Lei Shao and Seppo Louhenkilpi: Mathematical Modeling of Nitrogen Removal from the Vacuum Tank Degasser, accepted for publication in *Steel Research International.*

Author's Contribution

The author of this thesis is the main contributor of the papers presented above. She has conducted extensive literature survey on the related field and written the draft of each paper, which has been later revised by the author and her supervisor. Also, the author developed the CFD model described in the papers and all the CFD simulations were performed by her in the past years.

List of Symbols and Abbreviations

Symbols

A	Area
a	Interfacial area concentration
C	Coefficient
c	Concentration
D	Diffusivity
d	Diameter
F	Force
Fr	Froude number
f'	$= \left(1 - \alpha_p\right)^{1.5}$
f	Activity coefficient
G	Production
g	Acceleration of gravity
H	Bath height
J	Flux
K	Equilibrium constant
k	Turbulent kinetic energy
k'	Chemical reaction rate constant
L	Bath depth
M	Mole mass
P	Pressure
Q	Gas flow rate
R	Ladle radius or gas constant
Re	Reynolds number
S	Source term
r	Radial distance
t	Time
U	Velocity
u	Velocity
V	Volume
w	Velocity perpendicular to the free surface
X	Dissolved impurity (i.e. hydrogen or nitrogen)
x	x direction
Y	Species mass fraction
α	Volume fraction
γ	Activity coefficient in the infinite dilution
ε	Turbulent dissipation
θ	Relaxation time
κ	Mass transfer coefficient
λ	Instability wave length
μ	Viscosity or chemical potential
ν	Kinematic viscosity
π	Constant
ρ	Density
φ	Variable index

Subscripts

cv	Control volume
b	Bubble
cap	Strongly deformed regime
D	Drag
dis	Distorted bubble regime
e	Equilibrium
eff	Effective
fs	Free surface
g	Gas
hyc	Hydraulic
[H]	Hydrogen in steel
i	Species
inlet	Inlet
k	Turbulent kinetic energy
L	Lift
l	Liquid
m	Molecular
max	Maximum
md	Modified
mix	Mixture
[N]	Nitrogen in steel
nozzle	Nozzle
p	Phase p

pq	Interaction between phase p and phase q
q	Phase q
RC	Random collision
RT	Rayleigh-Taylor
TI	Turbulent impact
t	Turbulence
vis	Viscous regime
WE	Wake entrainment
X	Concerned element (i.e. H or N)
ε	Turbulent dissipation

Superscripts

m	Mass transfer
r	Chemical reaction

Abbreviations

CFD	Computational Fluid Dynamics
IAC	Interfacial Area Concentration
RH	Ruhrstahl Heraeus Recirculation degassing process
TKE	Turbulent Kinetic Energy
VTD	Vacuum Tank Degasser

Table of Contents

1. Introduction

In modern steelmaking, the demand for clean steels has been consistently growing throughout the industry as improvements to steel's mechanical properties play a vital role in defending steel products against newer competitive materials. Steelmakers are urged to precisely control the temperature and composition of liquid steel in order to produce ultra-clean steels with low contents of impurities, such as sulfur, phosphorus, non-metallic inclusions, hydrogen and nitrogen. It is well known that dissolved hydrogen has a number of negative effects on the processing characteristics and service performance of steel products. For example, if liquid steel contains an excessive amount of hydrogen, significant quantities of hydrogen could be ejected during solidification - since the solubility of hydrogen in steels declines with a decrease in temperature - resulting in pinhole formation and porosity in steel products. In fact, just a few parts per million of hydrogen dissolved in steels would cause severe hairline cracks, tensile ductility loss, hydrogen embrittlement and blistering. In the case of nitrogen, it can be either a detrimental or a beneficial element depending on the other alloying elements present, the form and quantity of nitrogen present, and the required steel grade. For instance, nitrogen is effective in improving the mechanical and corrosion properties of steels if it remains in solid solution or precipitates as very fine and coherent nitrides [1]. In general, however, nitrogen in most steel products is regulated within a limited level because high nitrogen content may cause poor cold formability and inconsistent mechanical properties (especially in hot-rolled products).

1.1. Vacuum Tank Degasser

In order to obtain a satisfactory cleanliness of steels, it is necessary to control and improve a wide range of operating conditions throughout the steelmaking process like deoxidant and alloy additions, secondary metallurgy treatments, shrouding and casting strategies. In practice, degassing treatment of liquid steel has allowed steelmakers to produce products with low contents of carbon, hydrogen and nitrogen. There are basically two types of degassers, one is called the recirculating process, such as the RH degasser in which liquid steel is recirculated from a lower ladle into an upper degassing unit and back to the ladle. The other type is referred to as the simple ladle or tank degasser, where a vacuum atmosphere is applied and inertial (argon) gas is bubbled through the melt. The scope of the present thesis is limited to the vacuum tank degasser (VTD), which is schematically illustrated in **Figure 1.1**. As can be seen, a refractory lined ladle is placed in a chamber where the ascending gas is pumped out, leading to a very low operating pressure inside the chamber (i.e., less than 1 mbar). At its bottom, the ladle is equipped with porous plug(s) or nozzle(s) where argon gas is blown in. It should be noted that in the chamber cover there is an addition hopper with a vacuum lock (*cf.* **Figure 1.1**) which is used to add alloying elements and/or slag components during vacuum treatment. In fact, the vacuum tank

degasser is quite prevalent in today's steelmaking industry as in addition to its degassing functions it can also offer more benefits, e.g., desulphurization, non-metallic inclusions removal, precise alloying, and temperature and composition homogenization. The following text will however, place most emphasis on the degassing process in the VTD as it has been the primary focus of this thesis work.

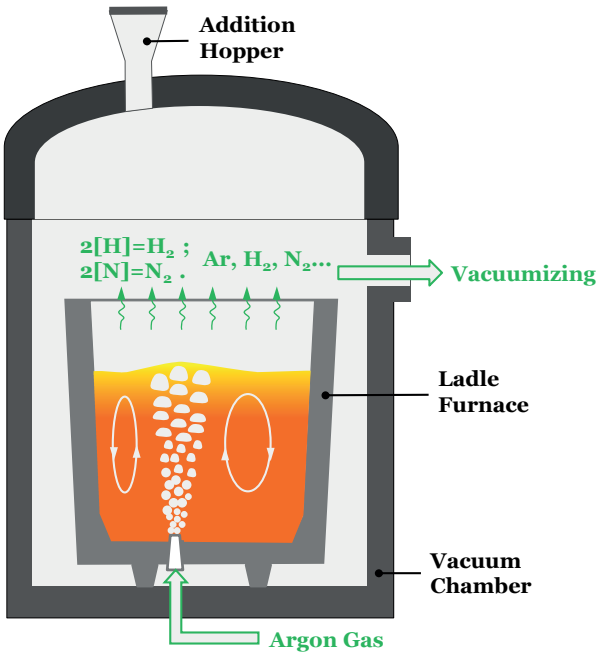

Figure 1.1 Sketch of a vacuum tank degasser

Gas removal in a VTD is mainly accomplished by the following reaction:

$$[\mathrm{X}] = \frac{1}{2}\mathrm{X}_2 \tag{1.1}$$

where X denotes the dissolved impurity (i.e., hydrogen or nitrogen).

According to the Sievert's law, a general equilibrium relation can be written for the above reaction:

$$c_{[\mathrm{X}]} = \frac{\sqrt{P_{\mathrm{X}_2}}}{f_{[\mathrm{X}]} K_{\mathrm{X}}} \tag{1.2}$$

where c, f, P and K are respectively, the equilibrium concentration and activity coefficient of the concerned element, its partial pressure in gas atmosphere and equilibrium constant that only depends on the operating temperature.

Evaluation of Eqn. (1.2) shows that from a thermodynamic point of view a very low and completely satisfactory level of hydrogen or nitrogen in molten steel can be obtained under vacuum conditions. However, such a low level would, in reality, take a very long time even if it is not impossible due to kinetic limitations. In practice, a considerable amount of purge bubbles (generated from gas injections) are introduced to stir the liquid bath and to prompt degassing reactions at numerous local sites.

1.2. Computational Fluid Dynamics (CFD) Approach

Computational Fluid Dynamics (often abbreviated as CFD) principally belongs to a branch of fluid mechanics and adopts numerical methods and algorithms to solve and analyze diverse issues involving fluid flows. The fundamentals of all CFD problems are the Navier-Stokes equations in conjunction with a set of auxiliary expressions derived from theoretical and/or experimental investigations. Over the years, principally due to the rapid evolution of computer techniques, various methods have been developed to discretize computational domains and to linearize underlying equations. Nowadays, by employing a supercomputer or cluster, large-scale simulation scenarios with multiphase interactions can be performed within an acceptable period of time.

Steelmaking is a complex process that involves the refining of hot metal in furnaces and ladles followed by solidifying through continuous casters. Of these, the refining operations generally encounter heat and mass transfers which are significantly associated with the state of flow motions in the metallurgical reactors (e.g. a VTD). Direct observations and measurements conducted in these vessels appear to provide useful insight into the system, which is practically impossible otherwise because the in-situ environments are always hostile and highly aggressive. Over recent decades, almost all the studies pertaining to ladle refining have been carried out by using CFD approaches and/or physical (aqueous) models. Compared to physical modeling, numerical approaches have received more attention mostly due to its incomparable advantages: like the relative ease with which complex processes of high temperatures and large-scale dimensions can be represented. Also, there is no inaccessible location in a computational domain and no disturbance caused by a probe, which are commonly encountered in a physical model [2].

1.3. Objective and Structure of the Thesis

The vacuum degasser is commonly utilized in the modern steelmaking industry and its importance to high-quality steel production has been highlighted by many researchers. In addition, due to the extensive research in this field, the prevailing conditions of fluid flow, mass/heat transfer and chemical kinetics are understood to a large extent. The present thesis has been aimed at examining the degassing phenomena (dehydrogenation and denitrogenation) in different operational VTDs and to provide VTD managers and operators with a versatile tool for better understanding the process and optimizing some operating parameters. To this end, a comprehensive CFD model has been developed step by step during the thesis work. A variety of elaborate sub-models and concepts, which are relatively separate in the literature, have been integrated into the CFD model. The multi-component effect of steel composition on the degassing process has been assessed by coupling the CFD model with an in-house thermodynamics code, which can be used to calculate the activity coefficient of dissolved elements in liquid steel as a function of steel composition and temperature. Also, efforts were put into developing an "*on-line use*" concept to control the nitrogen removal since CFD calculations are often time-consuming and are therefore, so far, inappropriate for on-line use.

The summary of this thesis contains a brief literature review on various investigations and modeling methods related to this field. Three VTDs from different industri-

al plants are briefly described in terms of their geometric configurations and main operating conditions. Finally, the CFD models established in the thesis are illustrated by outlining a few examples.

2. Literature Review

The whole operation of VTDs encompasses a variety of intricate processes and today, thanks to extensive work conducted internationally, the general principles with regard to VTDs have been elucidated to a significant extent. A VTD is essentially a system comprising of a gas-stirred ladle operated under reduced pressure, therefore, some research and modeling methods used to investigate the phenomena pertaining to gas-stirred ladles are summarized and discussed in this chapter. Overall, the focus is put on models and methods closely related to the work presented in this thesis.

2.1. Hydrodynamics of Gas-stirred Ladles

Hydrodynamic behaviors of gas-stirred ladles have been mostly clarified by many researchers: **Figure 2.1** shows a simplified outline of the hydrodynamics that can occur within gas-stirred ladles. As the gas is injected into the heavier surroundings (i.e., liquid steel), it expands quickly due to the sudden change of pressure and temperature. The resulting gas envelopes break into numerous bubbles rapidly over a very short distance from the bottom and the bubbles with different sizes proceed vertically upwards [3]. As a result, the liquid steel around the bubbles is accelerated and forced to move upwards following the bubbles. This motion can then be transferred to the steel bulk near the bubble-steel mixture region by viscous force and lateral turbulent fluctuations, leading to a recirculating flow in the ladle (*cf.* **Figure 2.1**). When the bubble-steel mixture reaches the bath surface, bubbles break through to the atmosphere and the momentum of the liquid stream is transformed into a radially spreading surface flow.

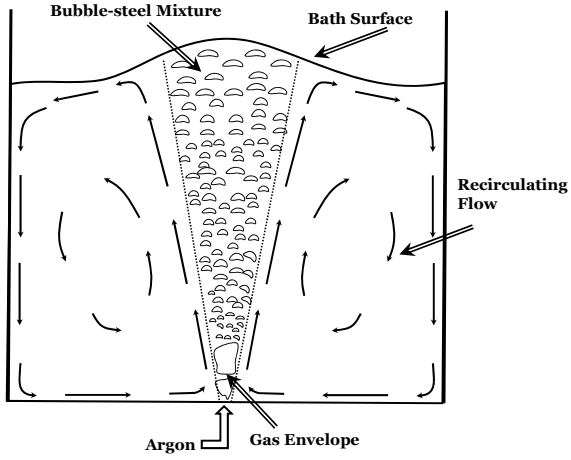

Figure 2.1 Schematic of hydrodynamics in a gas-stirred ladle

2.1.1. Gas-liquid plumes

The basic feature in the aforementioned gas-stirred ladle system is the bubble-steel mixture (*cf.* **Figure 2.1**), which by its very hostile and highly aggressive nature, makes direct observations and measurements on an industrial ladle extremely cumbersome and costly if not impossible. Instead, characteristics of the process have been widely investigated by using aqueous systems since water and liquid steel have equivalent kinematic viscosities [4-10]. It should be stressed that in industry small ladles are equipped with one bottom plug and large ones with two, which typically have non-axisymmetric geometries with eccentric injections. However, the physical models that have been used for fundamental studies were mostly equipped with axisymmetric nozzles/orifices for the sake of simplicity.

It is now generally accepted that the mixture region (*cf.* **Figure 2.1**) assumes a truncated conical shape as flow conditions in the ladle reach a relatively steady state. Based on experimental investigations, the gas dispersion region has been divided into four distinct regimes, namely: primary bubble, free bubble, plume and spout. Of these, the influence of kinetic energy induced by the gas injection eventually decays in the primary and free bubble regimes, whilst, in contrast, the plume region is solely governed by buoyancy due to large density difference between the two phases. Anagbo and co-workers [8] were probably the first who quantitatively demarcated the depth of each regime in a liquid bath by deriving a dimensionless dispersion group, N_D, based on extensive data from different gas-liquid systems. The authors further implied that the plume can occupy most of the bath depth under the practical (moderate) gas flow rates adopted in ladle operations. This essentially proves that assuming the presence of a buoyant plume to describe the fluid dynamics in metallurgical gas-stirred ladles is quite reasonable [3].

Gas volume fraction, bubble frequency and rising velocity within the plume have also been measured and studied by numerous investigators in vessels of widely varying dimensions and operating parameters [6-14]. As a rule, computer aided resistivity probes were utilized to measure the variables and the results of these studies [6, 9-10] indicate that the normalized radial profile of a gas volume fraction is Gaussian and consequently, the fully spatial gas fraction (α) distribution in the plume can be expressed using the following dimensionless form:

$$\frac{\alpha_g}{\alpha_{g,max}} = \exp\left(-0.7\left(\frac{r}{r_{max/2}}\right)^{2.4}\right) \tag{2.1}$$

where $\alpha_{g,max}$ is the locally maximum gas volume fraction, r is the radial distance and $r_{max/2}$ is the distance from the symmetric axis to the position where gas fraction is half the maximum value.

It has also been shown that, with the exception of the bath surface and the immediate vicinity of the gas injection point, the (average) bubble rising velocity within the plume is somewhat independent of the vertical height of the bath [6, 9]. These observations confirm that hydrodynamic conditions in the vicinity of the gas entry are of less importance to the gas-stirred system and the initial momentum of the gas jet can be neglected when conducting mathematical and/or numerical analysis.

2.1.2. Flow field outside the plume

In addition to the measurements of various parameters within the plume region, gas-stirred flows outside the plume have also been determined and investigated. The liquid velocities have generally been measured by using a laser anemometer or Doppler velocimetry in water models with different injection arrangements, *i.e.* nozzles or (porous) plugs [5, 9-11]. **Figure 2.2** depicts the measured (mean) velocity profiles in the bulk liquid, which have been carried out at the beginning of 1980s [5]. As it shows, a big vortex of recirculating flow occurs in the upper half of the bath and some quiescent zones exist at the bottom portion of the ladle, which is a typical flow pattern in such a system. Subsequent measurements made by employing more advanced and accurate devices have confirmed the flow pattern and further revealed that a relatively high vertical velocity at the plume axis is readily apparent [10].

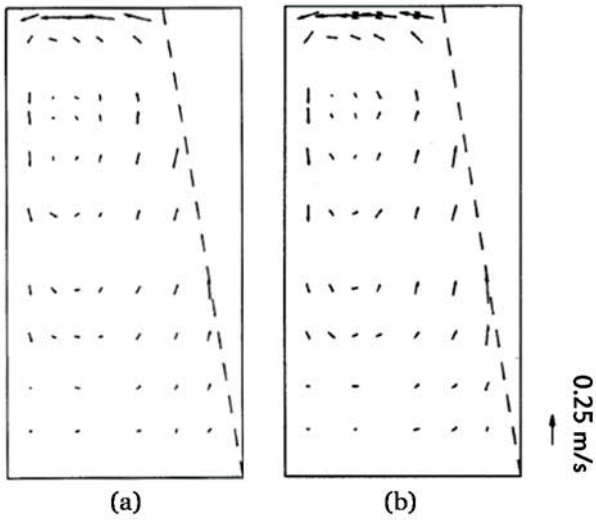

Figure 2.2 Experimentally measured velocity profiles for a gas velocity of (a) 1.6 m/s and (b) 3.2 m/s at the injection nozzle [5]

Sahai and Guthrie [12] were among the first to correlate the average speed of liquid recirculation to key operating parameters in gas-stirred ladles on the basis of energy balance analysis. Latterly, some of the approximations and simplifications made by the authors have been questioned and several modifications have been proposed by Mazumdar and coworkers [13, 14]. Through their improvements these authors arrived at an explicit expression for the mean recirculation speed, U, in terms of some key operating variables:

$$U = 0.86\frac{Q^{0.33}L^{0.25}}{R^{0.58}} \tag{2.2}$$

where Q, L and R are the gas flow rate, (equivalent) bath depth and ladle radius.

2.1.3. CFD modeling approaches

The state of fluid motion has considerable influence on secondary steelmaking processes due to the significant impacts on mixing efficiency, mass and heat transfer,

inclusion removal and refractory wear. Therefore, extensive fundamental studies and diverse CFD simulations of fluid flow in gas-stirred ladles have been previously carried out as the gas injection induced flow is mostly encountered in secondary steelmaking. Szekely and coworkers outlined the first ever CFD model of a gas-stirred system by solving the turbulent Navier-Stokes equations [4]. The authors assumed that the plume comprised of a cylinder shape and that the bulk flow was driven by shear stress between gas and liquid. Although these assumptions have been shown to be unrealistic, this work has pioneered the development of computer aided process metallurgy, giving rise to an exponential increase in publications adopting CFD techniques. Of these, three approaches are commonly applied in the open literature, namely, quasi single-phase, Lagrangian-Eulerian and Eulerian-Eulerian. The distinctive features and calculation procedures of these techniques are briefly summarized in the following text. It is worth noting here that for all CFD simulations containing process variables (e.g. molten liquids and high temperature) the gas flow rate has to be converted from the 'standard state' to a certain in-situ state, for which the ideal gas law has commonly been applied in the literature.

2.1.3.1. Quasi single-phase approach

The quasi single-phase model is basically a continuum approach, in which the gas-liquid mixture within the upwelling plume is treated as a homogeneous liquid with reduced density. This approach has been widely used, e.g. by the groups headed by Szekely and Guthrie [4, 5, 13-17], particularly in the earliest applications of CFD to such processes. The CFD models utilized in the above mentioned reports were all two-dimensional based on the axisymmetric coordinate (primarily due to limited computing capabilities) and **Figure 2.3** illustrates the basic calculation procedures.

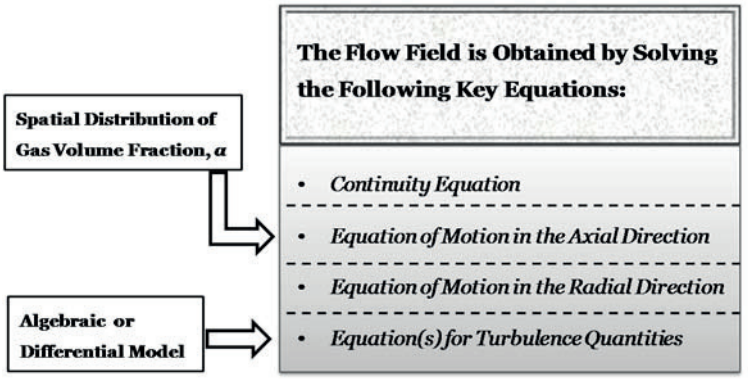

Figure 2.3 Calculation procedures of the quasi single-phase approach

As shown in the figure, the key to the numerical approach is a set of conservative equations and more importantly, the (spatial) distribution of gas volume fraction and turbulence quantity calculation method should be specified before the equations are solved. These conservative equations are comprehensively described in Ref. [2] and therefore, are not reproduced here. The gas volume fraction embodied in the axial momentum equation is required to represent the buoyancy force (per unit volume), through which the recirculating flow is generated. On the other hand the turbulence model is used to compute the effective viscosity that is embodied in each momentum

equation. It has been recognized that a good estimate of effective viscosity is a prerequisite for successfully predicting flow conditions in the two-phase system [14]. The gas volume fraction can be specified on the basis of either auxiliary expressions or experimental measurements. For instance, both slip and non-slip models have been proposed and assessed by different investigators, who concluded that a reasonable agreement between measured and calculated flow fields can be achieved by assuming slip between gas and liquid phases [15, 18]. In some later work, the measured gas voidage and plume geometry were implemented in the numerical approach [10, 19]. Zhu *et al.* [20] conducted a numerical study for the turbulent fluid flow and mixing characteristics in gas-stirred ladles by using a three-dimensional code, which was developed on the basis of the quasi single-phase approach. The code has been proven to be more advanced than the previous ones since it can account for both an axisymmetric system and an eccentric bubbling ladle. The effects of gas flow rate, nozzle arrangement at the bottom and sidewall pattern of the ladle on fluid flow phenomena were investigated in the study and very informative conclusions have been drawn: A ladle with (slightly) tapered sidewalls has shorter mixing time compared with a cylindrical one and eccentric blowing increases the azimuthal velocities in a ladle (*cf.* **Figure 2.4**), thus reducing the mixing time.

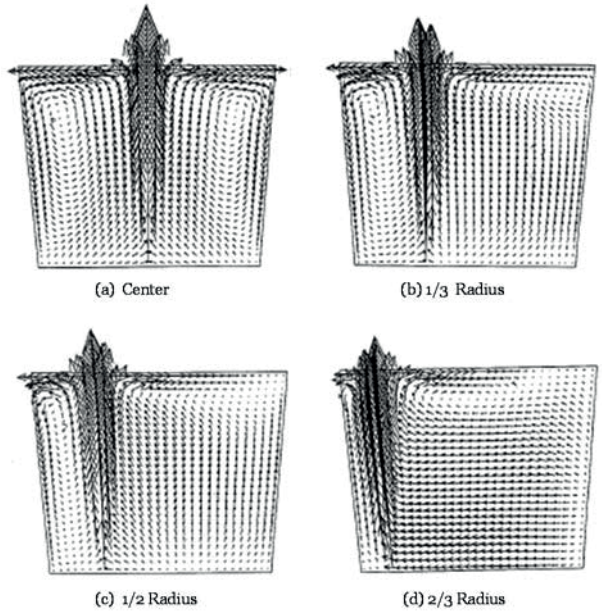

Figure 2.4 The computed flow fields on the symmetric plane with different nozzle arrangements [20]

The quasi single-phase approach is by far the most simplistic and computationally efficient for modelling fluid flow in gas-stirred ladles. Good correlations have been achieved between the numerical simulations and physical experiments in terms of flow field, mixing time and turbulence quantity distribution. However, due to the assumption of homogenization, it is impossible to account for the interfacial phenomena that are of great importance to the steelmaking modellers by using such an approach. As a result, a simulation model based on a two-phase approach is required

despite the obvious increase of model complexity and this has led to the subsequent development of Lagrangian-Eulerian and Eulerian-Eulerian approaches.

2.1.3.2. Lagrangian-Eulerian approach

In the Lagrangian-Eulerian approach, the trajectories of a stream of (particulate) bubbles are calculated in a Lagrangian field, whereas the bulk liquid motion and turbulence parameters are calculated with a fixed Eulerian grid. Johansen and Boysan [21] were among the first to introduce the approach to simulate the fluid dynamics in a gas-stirred ladle. The authors stressed that as the quasi single-phase approach lacks generality because the movement and spread of the bubbly plume are given a priori according to some experimental observations and measurements an alternative approach was required. They presented a special calculating procedure to solve the equations of liquid flow (and turbulence) coupled with the motion of gas bubbles, thus predicting mean flow velocities, bubble dispersions, buoyancy effects and mass transfer rates from first principles. Later on, Mazumdar and Guthrie [22] simulated submerged gas injection phenomena during ladle refining operations by adopting a similar calculating procedure, briefly described as follows:

(a) The bubble motion equations are solved (first by using a 'null' set of flow velocity and turbulence and later, using the updated ones). The predicted bubble trajectories are superimposed on to the Eulerian grid and the overall distributions of gas volume fraction and interfacial drag forces are estimated.

(b) The estimated gas volume fraction and interfacial drag forces are then incorporated into the continuous phase equations (i.e., liquid flow and turbulence) that are solved iteratively. Typically, a large number of iterations were performed before re-solving the trajectories.

(c) At the end of the predetermined number of iterations, bubble trajectories are re-calculated using the prevalent flow and turbulence fields as well as the updated distributions of gas volume fraction and interfacial drag forces.

(d) The sequences from step (a) to (c) are repeated until a converged solution is reached.

It must be noted that in the above mentioned reports the authors assumed that only mono-size bubbles are present in the system and bubble-bubble interactions were totally ignored. In addition, only the drag force induced by velocity difference was considered in the bubble motion equations, which could explain the general deviations between the measurements and predictions especially in the vicinity of the gas injection nozzle and the free surface (*cf.* **Figure 2.5**).

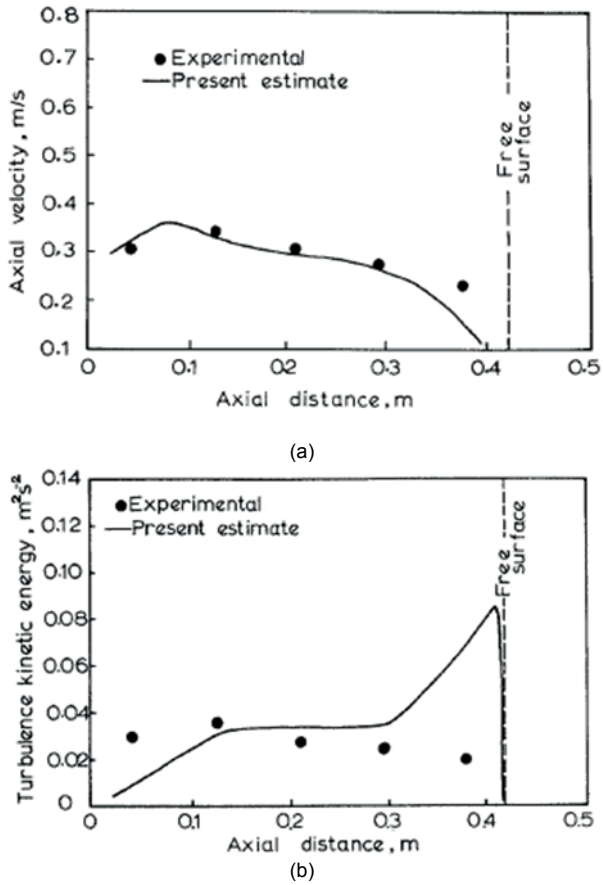

Figure 2.5 Comparisons of numerical predictions and the corresponding experimental measurements along the axial distance. (a) Axial velocity; (b) Turbulence kinetic energy [22]

Guo and Irons [23] conducted a numerical study based on the Largrangian-Eulerian principles where different body and interfacial forces embodied in the bubble motion equations were taken into account, i.e., the virtual mass force, buoyancy force, drag force and lift force. It has been shown that the predictions compare very well with available experimental results in Wood's metal [24, 25] in terms of plume geometry, gas voidage and liquid velocity. More importantly, it has been demonstrated that the lateral lift force is responsible for plume spreading while the drag force induces its bending towards the ladle sidewall. Olsen and Cloete [26] have also presented an advanced model for simulating hydrodynamics of gas-stirred ladles in which the overlaying liquid phase was modeled by utilizing the volume of fluid method and a combined correlation describing the lift coefficient was evaluated. The calculated results showed that at a high gas flow rate the assumption of a flat free surface on the bath top is still valid but the effect of lift force is minor.

Cloete [27] argued that a more realistic plume can be predicted based on a large number of accurate auxiliary correlations and approximations. For example, a drag law for spherical capped bubbles, a turbulent dispersion model, an algorithm accounting for particle (i.e., bubble) growth and breakup and a pre-defined bubble size distribution. To this end, the author outlined a full scale, three-dimensional and tran-

sient numerical model to simulate fluid flow and mixing in gas-stirred ladles. The model was employed to assess various operating and design parameters pertaining to flow field and mixing efficiency by conducting systematic studies. The predicted plumes in the ladle under different gas flow rates are outlined in **Figure 2.6**, where the theoretical profiles proposed by Oeters et al. [28] are also plotted.

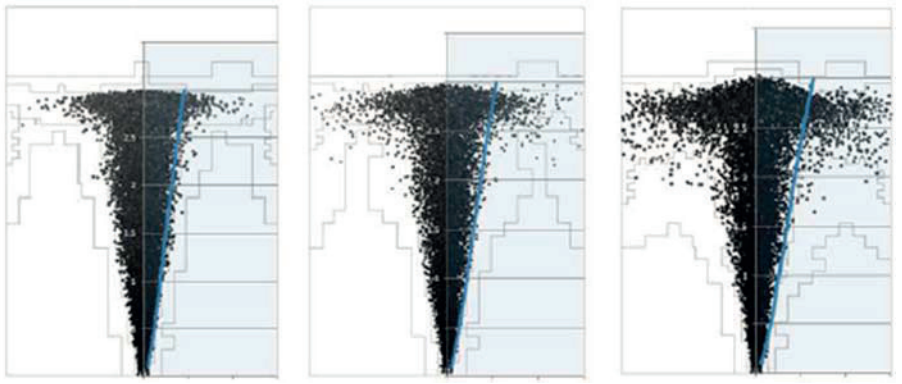

Figure 2.6 Comparisons of predicted plume representations and the theoretical ones (blue lines) [27]

The Largrangian-Eulerian approach has proved to be very promising in simulating the bubble driven flow in gas-stirred ladles and has gained ample attention over recent years. The model also has a large potential to provide a platform for investigations on other fundamental but significant issues, e.g., alloying element dissolution, non-metallic inclusion behavior and degassing phenomena. The main disadvantage of the approach lies in the associated high computational demand or the limited bubble numbers that can be considered.

2.1.3.3. Eulerian-Eulerian approach

In contrast with the Lagrangian-Eulerian treatment, the Eulerian-Eulerian approach assumes that both phases may coexist in the same control volume at the same time and each phase consists of a continuous field interpenetrating and interacting with the other in the computational domain [2]. Consequently, the concept of phasic volume fraction is applied and continuity and momentum conservative equations embodying the volume fraction are solved for both the phases.

Schwarz and Turner [29] were among the first to simulate the two-phase turbulent flow in a gas-stirred bath by adopting the Eulerian-Eulerian method. The authors implemented extra turbulent diffusion terms in the continuity equations and only considered drag forces between the two phases, which were contained in the momentum equations. Ilegbusi and Szekely [30] later on reported a similar but three-dimensional model to calculate the turbulent recirculating two-phase flow both in an air-water and a nitrogen-steel system. The results showed that the predicted liquid velocities correlate well with the corresponding experimental ones and more interestingly, (nitrogen) gas plumes in molten steel appear to be much narrower and behave quite differently from those in water. The authors therefore concluded that more experimental work to evaluate their predictions and systematical studies to assess the influence of the various auxiliary correlations/coefficients are required. Based on the previous publication [31], Jonsson and Jönsson [32] presented a more practical mod-

el that includes argon gas, slag as well as liquid steel in the ladle. The thermal effects on material properties including density, heat capacity and viscosity were also taken into account by solving energy conservation equations. The predicted surface velocities of steel were reported to be in at least five times greater agreement with experimental data compared to the ones in a model that excludes the effect of slag.

Over the years, a large amount of work has been conducted internationally for this purpose and several non-drag mechanisms of interfacial interaction have been integrated in the calculating procedures [33-42]. It is now commonly accepted that the momentum transfer between the phases is accommodated by a set of interfacial forces that are mainly categorized as drag force and non-drag forces. For the bubbly flow system, the non-drag forces generally include the (lateral) lift force, the virtual mass force and the turbulent dispersion force. The relative importance of each force depends on the bubble size and on the turbulence degree in the bath. In the literature, the drag force and lift force are usually considered to describe the plume bending and spreading, respectively, however, some or all of the other non-drag forces are ignored. Drag force acts on bubbles in the case they moved with a relative (slip) velocity within the surrounding liquid and as a consequence, the drag force always imposes in the opposite direction of this relative movement. Within the framework of the Eulerian-Eulerian approach, the drag force is composed of the following:

$$\vec{F}_{\mathrm{D}} = \frac{3\alpha_{\mathrm{g}}\alpha_{\mathrm{l}}\rho_{\mathrm{l}}C_{\mathrm{D}}}{4d_{\mathrm{g}}}\left|\vec{u}_{\mathrm{g}} - \vec{u}_{\mathrm{l}}\right|\left(\vec{u}_{\mathrm{g}} - \vec{u}_{\mathrm{l}}\right) \tag{2.3}$$

where α, ρ, d and u are the volume fraction, density and bubble diameter, respectively. The subscripts 'g' and 'l' denote the gas and liquid phase. C_{D} is the drag coefficient and there exists a variety of correlations implemented in the literature, as reviewed by Lou and Zhu [42].

Lift force is exerted on a bubble when there exists velocity gradients within the surrounding liquid. Pressure is lower in the region where the relative velocity is larger and the bubble is driven into this region due to the lift effect acting perpendicularly to the direction of the relative movement and the following formulation has been widely adopted:

$$\vec{F}_{\mathrm{L}} = -\alpha_{\mathrm{g}}\rho_{\mathrm{l}}C_{\mathrm{L}}\left(\vec{u}_{\mathrm{g}} - \vec{u}_{\mathrm{l}}\right) \times \left(\nabla \times \vec{u}_{\mathrm{l}}\right) \tag{2.4}$$

where C_{L} is the lift coefficient, which shows quite a variation throughout the literature and can be basically determined by comparing the numerical results against corresponding experimental measurements.

In a recent study, the hydrodynamics of a 60-ton industrial ladle was simulated using an Eulerian-Eulerian methodology [43]. As can be seen in **Figure 2.7**, the gas plumes are defined by plotting the iso-surfaces of gas volume fraction and the liquid flow is associated with two recirculating zones in each half of the symmetric plane. It has been reported by the authors that the magnitude of the liquid velocity is consistent with the one for equivalent industrial configurations.

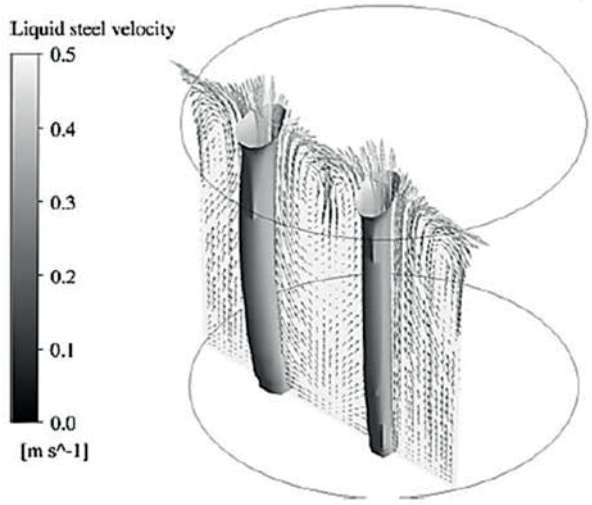

Figure 2.7 Predicted flow field of liquid steel and the argon plumes in a vertical plane passing through the porous plugs under a low gas flow rate [43]

A common approximation among the investigations mentioned above is that the bubble size is assumed constant throughout the bath and a representative value of diameter is usually given by a theoretically deduced or empirical expression. The value is then used to determine the drag force (coefficient) and some other related non-drag forces. Some of the authors pointed out that even a big change in bubble diameter has only a limited impact on the bubble plume and bulk liquid flow [40, 42]. Still, this approximation seems implausible since both bubble breakup and coalescence have been observed in physical experiments [8, 10]. A more reliable method is therefore required to calculate the bubble size distribution within the bath, which is an important parameter for predicting mass, momentum and energy transfers through the interface between gas and liquid in a gas-stirred ladle. To the best of the present author's knowledge, the only practical way to achieve this goal is to calculate the interfacial area concentration (IAC) by solving its transport equations. The IAC is defined as the total surface area of gas bubbles per unit (mixture) volume and the local bubble size can be readily computed. Kocamustafaogullari and Ishii [44, 45] were among the first to derive an IAC transport equation from the statistical model of particle number density one-dimensional case, which includes the source and sink terms due to particle breakup and coalescence. Some subsequent publications [46-49] showed a few variations of the original model to account for different sizes of bubble and in general, the simulated results have shown good correlation with the physical observations.

2.1.3.4. Turbulence considerations

The importance of turbulence transportation has been readily understood as it has been stressed that (turbulent) eddy diffusion is primarily responsible for dispersing various materials across the streamlines of convective bulk flows in a ladle. Taniguchi et al. [50] demonstrated that it is more suitable to formulate the volumetric mass-transfer coefficient between gas bubbles and liquid by using an eddy-cell expression, implying turbulent diffusion governs the mass transfer process in their experimental

system. Also, it has been determined that the generation of turbulence in a ladle can aid in inclusion agglomeration and float-up in the bath.

Over the years, different versions of turbulent viscosity have been applied, ranging from an algebraic equation to the *k*-*ε* model with special near-wall function [51]. Grevet and co-workers used their own detailed experimental data as a basis to suggest that the standard *k*-*ε* model is inadequate to realistically simulate the turbulence phenomena in a gas-stirred system [5], a fact which was later confirmed by Mazumdar et al. [14]. Johansen and Boysan [52], probably for the first time, modified the coefficients of the standard *k*-*ε* equations and the effect of turbulence induced by bubbles within the plume was included via an additional source term. It has been demonstrated that the numerical predictions for a water model of a ladle show very satisfactory quantitative agreement with corresponding experimental results. Since then, other source terms embodying gas-induced effects have been proposed and examined thoroughly [10, 30]. As a result, the estimates of flow field and turbulence quantities in a gas-stirred ladle have evolved from 'consistent trend' to 'satisfactory agreement' when compared to the experimental measurements. Nowadays, as a rule, adequate predictions of both flow field and turbulence quantities in a gas-stirred ladle can be obtained by introducing proper source terms to *k*-*ε* equations and/or carefully adjusting some coefficients embodied in the auxiliary formulas.

2.2. Kinetics of Degassing in Gas-stirred Ladles

The degassing of liquid steel subjecting to vacuum treatment was introduced in 1950s with the primary objective to lower the hydrogen content of liquid steel to prevent cracks in large ingots and subsequently the process was also used for lowering the nitrogen and oxygen (and carbon) contents [1]. As a result the emphasis of the following text is placed on describing the kinetics of dehydrogenation and denitrogenation in gas-stirred ladles and reviewing some important related studies.

From a theoretical standpoint, degassing occurs as a result of the following series of steps:

(a) The gaseous element, namely [X], diffuses from the bulk liquid to the interface of gas (bubble) and steel

(b) Chemical reaction takes place at the interface as $[X] = \frac{1}{2}X_2$

(c) The gas product X_2 diffuses from the interface to the bulk gas phase (*i.e.* in the bubbles)

Apparently, as depicted in **Figure 2.8**, the above kinetics are governed by different mechanisms including mass transfer in liquid steel, chemical reactions at the interface and mass transfer in the gas phase. Consequently, the rate of the degassing process can be controlled either by mass transfer or the rate of chemical reactions. In terms of the slowest step, the overall degassing rate could be limited by (a) mass transfer in liquid steel, (b) chemical reaction at the interface and (c) mass transfer in the bulk gas; however, if more than one kinetic step influences the rate, it is mix-controlled. It has been widely accepted that mass transfer of gas product in the bubbles is quite fast in a gas-stirred ladle. For dehydrogenation, chemical reaction at the interface is rapid under the high temperature and hydrogen removal rate is mainly

controlled by mass transfer in liquid steel, which has been confirmed in the literature. Detailed description of mathematical formulae and considerations for hydrogen refining are given, among others, by a Swedish research group [53, 54]. In addition, a new concept for on-line prediction of hydrogen and sulfur removal was proposed by the same group [55, 56]. In contrast with dehydrogenation, denitrogenation is mix-controlled by mass transfer in liquid steel and chemical reaction at the interface because of the existence of some surface-active elements in the liquid steel. For example, sulfur is surface-active and can block the interfacial site for chemical reaction and reduces its rate [57-60]. In order to accommodate the predictive models embodying transport equations and to better understand the degassing process, substantial research has been conducted in the past, mainly focused on mass transfer in liquid steel and interfacial chemical reactions (of denitrogenation).

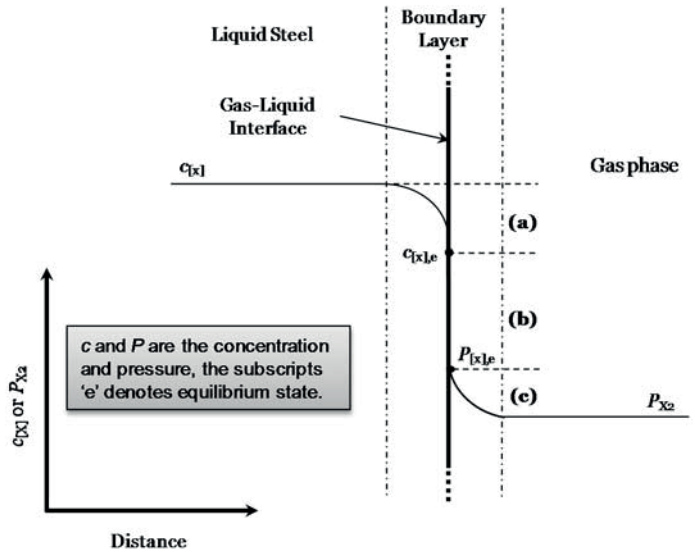

Figure 2.8 Illustration of degassing kinetics in gas-stirred ladles

2.2.1. Mass transfer in liquid steel

Mass transfer in a gas-stirred ladle occurs primarily as a result of molecular diffusion, turbulent diffusion and bulk convection. The total flux of a species 'i' across a fixed plane normal to the x-direction is therefore expressed as:

$$J_{\mathrm{i}} = -D_{\mathrm{m}}\frac{\partial c_{\mathrm{i}}}{\partial x} - D_{\mathrm{t}}\frac{\partial c_{\mathrm{i}}}{\partial x} + Uc_{\mathrm{i}} \qquad (2.5)$$

where D_{m} and D_{t} are the molecular diffusivity and eddy diffusivity, U is the average velocity. (It should be noted here that the three terms on the right hand side of Eqn. (2.5) accounts for molecular diffusion, turbulent diffusion and convection transport, respectively).

In normal ladle operations, the contribution of molecular diffusion to mass transfer in liquid steel is negligible and considerable efforts have been made to correlate the overall mass transfer coefficient to turbulence and flow parameters. To the best of the

author's knowledge, both the Higbie penetration assumption and the eddy-cell model have been frequently adopted in the literature to address these phenomena. Higbie assumed that mass transfer in a gas-liquid system is related to the surface renewal time, which is a function of bubble diameter and slip velocity [61]. Bannenberg and co-workers [59] employed the assumption to investigate degassing operations in secondary steelmaking and proposed that the mass transfer coefficient is proportional to the square root of diffusivity and depends on the hydrodynamics of the metal-gas system. Later on, Alves *et al.* [62] reported that the assumption is only applicable to systems at low dissipation of turbulent kinetic energy (TKE). On the other hand, the eddy-cell model postulates that mass transfer in gas-liquid system is mainly determined by the motion of small-scale eddies and thus the mass transfer coefficient is a function of TKE dissipation [63, 64]. Taniguchi *et al.* [50] for comparison used both a Higbie penetration expression and the eddy-cell model to determine CO_2 concentration in a water-CO_2 system. The results showed that the eddy-cell model is more accurate in the bubble dispersion region, where TKE dissipation is at a high level. Similarly, the numerical work conducted by Venturini and Goldschmit [41] indicated that the eddy-cell model based predictions agree satisfactorily with their experimental results both in a mass transfer (in liquid) controlled and a mix-controlled process.

2.2.2. Interfacial chemical reaction

The fundamentals of chemical reactions in steelmaking have been understood on the basis of laboratory experiments over the past decades. It has been revealed that steelmaking reactions are generally controlled by mass transfer at the boundary layers, e.g., dehydrogenation in gas-stirred ladles, due to the high temperature. However, there are exceptions, the most notable being absorption and desorption of nitrogen by liquid steel, which is a case of mix-controlled kinetics, i.e., both interfacial reaction and mass transfer partially control the overall reaction rate. This is because, as mentioned before, the surface-active elements in liquid steel can block the interfacial reaction sites, thus retarding the reaction rate.

Pehlke and Elliott [65] in their pioneering work measured the rates of nitrogen absorption and desorption by liquid iron and derived a number of very important findings: nitrogen absorption and desorption are approximately with the same rate constant and an increase in either oxygen or sulfur content in liquid iron drastically decreases the reaction rate. A subsequent study by Fruehan and Martonik [66] confirmed these findings and further showed that the rate of nitrogen absorption into Fe-Cr melts with low sulfur content is limited by mass transfer in the liquid phase. In contrast, for melts containing significant amounts of sulfur it is mix-controlled by both mass transfer and interfacial chemical reaction. As a result it is recommended that melts should be thoroughly deoxidized and desulfurized prior to subsequent processing by degassing units (*i.e.* a VTD).

Additionally, it has been reported that the operating temperature has a remarkable impact on denitrogenation rate in liquid steel, as Ito and co-workers [67] indicated from their experimental results that the effect of oxygen on nitrogen transfer rate decreases as the temperature of liquid steel increases, which leads to a lower oxygen fraction at the interface. Similarly, Fu *et al.* [68], demonstrated that the resistance of

sulfur to nitrogen removal rate decreases with increases in temperature. Harashima and co-workers [57, 58] investigated the kinetics of nitrogen desorption from liquid iron under reduced pressures. Their results showed that an increase in the total pressure gives rise to a reduced overall rate constant and the degree of negative influence of oxygen is about 2.5 times higher than that of sulfur. In addition they also managed to correlate the chemical reaction rate constant to oxygen and sulfur contents in liquid iron. Kitamura et al. [69] later on adopted this correlation and developed a mathematical model for nitrogen desorption in vacuum degasser. The predicted results agreed well with their experimental ones.

The effects of commonly encountered alloying elements on nitrogen behavior have also been extensively examined in the literature. Work by Choh *et al.* [70] revealed that manganese (Mn) and copper (Cu) in liquid steel may lower the interfacial temperature due to the latent heat of vaporization, thus decreasing the nitrogen removal rate. Other Japanese researchers argued that the elements such as titanium (Ti), zirconium (Zr), vanadium (V), manganese (Mn) and chromium (Cr), which have a stronger affinity with nitrogen than iron and as such would enhance the nitrogen dissociation rate, whereas the elements like aluminum (Al), silicon (Si), boron (B), copper (Cu), tungsten (W) and tin (Sn) impose a stronger repulsive force against nitrogen that would retard the dissociation rate [71-73].

3. Model Developed in the Thesis

As in "List of Publication and the Author's Contribution", four scientific papers are included as supplements in the thesis. The connections between the papers and their interactions with different industrial cases are briefly described in **Table 3.1**. **Paper I** presents the first version of the CFD model (i.e., M1.0), of which the main focus was put on evaluating different turbulence formulae to simulate the multiphase hydrodynamic phenomena in gas-stirred vessels. Also, a dehydrogenation module was included in M1.0 and it was employed to mimic hydrogen removal from an industrial vacuum tank degasser (i.e., Riva cases). As reported in **Paper II**, M1.0 was later on upgraded to M1.1 by introducing a denitrogenation module. The applicability of M1.1 was confirmed by simulating hydrogen and nitrogen removal from the Ruukki degasser. By considering the fact that sulfur in liquid steel can be removed by the overlaying slag, a desulfurization sub-module was coupled to M1.1 and this leads to the complete version (M1.2) of the CFD model established during the thesis work. As in **Paper III**, the versatility and applicability of M1.2 were explicitly shown. The efforts behind **Paper IV** were put into developing an "on-line use" concept to control the nitrogen removal and M1.2 was employed to conduct extensive simulations based on which two 3D operating diagrams were plotted.

Table 3.1 Connections between the supplement papers and the interactions with industrial cases

	Main feature	Task completed
Paper I	M1.0 ▪ Gas-liquid flow field ▪ Dehydrogenation	⇨ Validated by a water model from the literature ⇨ Applied on an industrial cases of Riva to simulate dehydrogenation
Paper II	M1.1 (based on M1.0) ▪ Denitrogenation ([S] is fixed)	⇨ Applied on industrial cases of Ruukki to simulate ○ Dehydrogenation ○ Denitrogenation
Paper III	M1.2 (based on M1.1) ▪ Denitrogenation ([S] varies during operation)	⇨ Applied on industrial cases of Ruukki to simulate ○ Denitrogenation including the effect of ▪ Desulfurization ▪ Alloying elements
Paper IV	M1.2	⇨ Applied on industrial cases of Ruukki to simulate ○ Denitrogenation emphasizing on building ▪ 3D operating diagrams for on-line use

Figure 3.1 schematically illustrates the structure and calculating procedures of the CFD model developed in this thesis. As can be seen, the model consists of a multiphase flow and a degassing sub-model. The former is based on the Eulerian-Eulerian approach and both the extended k-ε turbulence and one-group interfacial area con-

centration transport equation are embodied in the sub-model. Steady-state flow fields and IAC distributions are therefore obtained by solving the multiphase sub-model and then the results can be used by the degassing sub-model: By giving the correlations of mass transfer coefficient and chemical reaction rate constant, the species transport equation is solved to investigate the dehydrogenation and/or denitrogenation processes in a vacuum tank degasser.

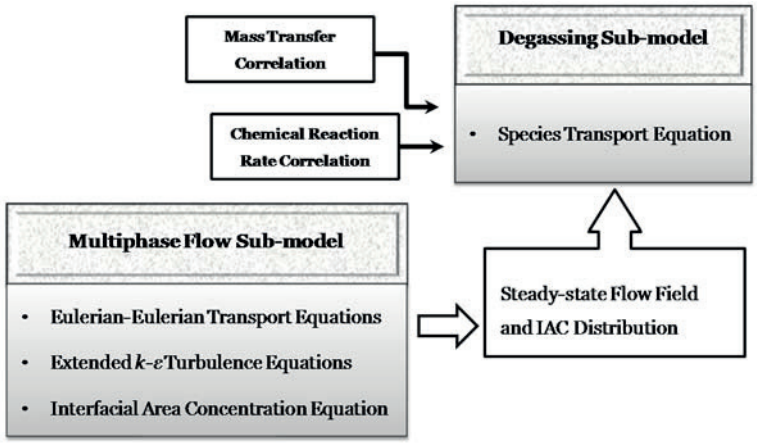

Figure 3.1 Schematic of model structure in the thesis

3.1. Conservation Equations

The main conservation equations including Eulerian-Eulerian transport equations for gas-liquid flows, extended k-ε equations, interfacial area concentration and species transport equations are expressed as follows.

3.1.1. Multiphase flow

The continuity equation for phase 'q' (i.e., gas or liquid steel) is:

$$\nabla \cdot \left(\alpha_{\mathrm{q}} \rho_{\mathrm{q}} \vec{u}_{\mathrm{q}}\right) = 0 \tag{3.1}$$

where α, ρ and $\vec{u_{\mathrm{q}}}$ are the volume fraction, density and velocity vector, respectively.

The momentum equation for phase 'q' is defined as:

$$\nabla \cdot \left(\alpha_{\mathrm{q}} \rho_{\mathrm{q}} \vec{u}_{\mathrm{q}} \vec{u}_{\mathrm{q}}\right) = -\alpha_{\mathrm{q}} \nabla P + \nabla \cdot \left(\alpha_{\mathrm{q}} \mu_{\mathrm{eff,q}} \nabla \vec{u}_{\mathrm{q}}\right) + \alpha_{\mathrm{q}} \rho_{\mathrm{q}} g + \vec{F}_{\mathrm{L,pq}} + \vec{F}_{\mathrm{D,pq}} \tag{3.2a}$$

where P and μ_{eff} are the pressure and effective viscosity, the subscript 'p' stands for the phase other than phase 'q'.

The lift force $\vec{F}_{\mathrm{L,pq}}$and drag force $\vec{F}_{\mathrm{D,pq}}$ are considered between gas (bubbles) and liquid steel in the model, and are expressed as:

$$\vec{F}_{\mathrm{L,pq}} = -C_L \alpha_{\mathrm{q}} \rho_{\mathrm{q}} \left(\vec{u}_{\mathrm{p}} - \vec{u}_{\mathrm{q}}\right) \times \left(\nabla \times \vec{u}_{\mathrm{q}}\right) \tag{3.2b}$$

$$\vec{F}_{\mathrm{D,pq}} = C_{\mathrm{D}} \frac{\alpha_{\mathrm{q}} \alpha_{\mathrm{p}} \rho_{\mathrm{p}} \mathrm{Re}}{24\theta} \left(\vec{u}_{\mathrm{p}} - \vec{u}_{\mathrm{q}}\right) \tag{3.2c}$$

where C_{L} and θ are the lift coefficient and bubble relaxation time, respectively. The drag coefficient C_{D} is determined by the following expressions:

$$C_{\mathrm{D}} = \begin{cases} C_{\mathrm{D_{vis}}} = \dfrac{24}{\mathrm{Re}}(1 + 0.1\mathrm{Re}^{0.75}) & C_{\mathrm{D_{dis}}} < C_{\mathrm{D_{vis}}} \\ C_{\mathrm{D_{dis}}} = \dfrac{2d_{\mathrm{b}}}{3\lambda_{\mathrm{RT}}}\left(\dfrac{1 + 17.67f^{6/7}}{18.67f}\right)^2 ;\ f' = \left(1 - \alpha_{\mathrm{g}}\right)^{1.5} & C_{\mathrm{D_{vis}}} < C_{\mathrm{D_{dis}}} < C_{\mathrm{cap}} \\ C_{\mathrm{D_{cap}}} = \dfrac{8}{3}\left(1 - \alpha_{\mathrm{g}}\right)^2 & C_{\mathrm{D_{cap}}} < C_{\mathrm{D_{dis}}} \end{cases} \tag{3.2d}$$

where d_{b} and λ_{RT} are the bubble diameter and Rayleigh-Taylor instability wavelength.

3.1.2. Extended *k*-*ε* equations

The standard *k*-*ε* (mixture) equations for turbulence calculation are expressed as:

$$\nabla \cdot (\rho_{\mathrm{mix}} k \vec{u}_{\mathrm{mix}}) = \nabla \cdot \left(\frac{\mu_{\mathrm{t,mix}}}{\sigma_{\mathrm{k}}} \nabla k\right) + G_{\mathrm{k}} - \rho_{\mathrm{mix}} \varepsilon + S_{\mathrm{k}} \tag{3.3a}$$

$$\nabla \cdot (\rho_{\mathrm{mix}} \varepsilon \vec{u}_{\mathrm{mix}}) = \nabla \cdot \left(\frac{\mu_{\mathrm{t,mix}}}{\sigma_{\varepsilon}} \nabla \varepsilon\right) + \frac{\varepsilon}{k}(C_{1\varepsilon} G_{\mathrm{k}} - C_{2\varepsilon} \rho_{\mathrm{mix}} \varepsilon) + S_{\varepsilon} \tag{3.3b}$$

where the subscript 'mix' denotes mixture (volume-averaged) quantity, μ_{t} and G_{k} are the eddy viscosity and production of turbulence kinetic energy (TKE). S_{k} and S_{ε} are the source term (i.e., zero by default).

The above (standard) equations should not be directly applied in the gas-liquid system where the bubbles could magnify turbulence in the bulk liquid as a result of interfacial interactions like drag, wake shedding and bubble wobbling. In order to take such aspects into account, the standard equations have been extended by Sheng and Irons [10]. The source terms suggested by the authors are:

$$S_{\mathrm{k}} = C_{\mathrm{k1}} \alpha_{\mathrm{g}} (1 - \alpha_{\mathrm{g}}) G_{\mathrm{k}} + C_{\mathrm{k2}} C_{\mathrm{f}} \alpha_{\mathrm{g}} \rho_{\mathrm{l}} k \tag{3.3c}$$

$$S_{\varepsilon} = C_{\varepsilon 1} \alpha_{\mathrm{g}} (1 - \alpha_{\mathrm{g}}) G_{\mathrm{k}} \frac{\varepsilon}{k} + C_{\varepsilon 2} C_{\mathrm{f}} \alpha_{\mathrm{g}} \rho_{\mathrm{l}} \varepsilon \tag{3.3d}$$

where the subscripts 'l' and 'g' stand for liquid and gas phase, respectively.

3.1.3. Interfacial area concentration

A one-group IAC equation, which has been comprehensively described by Wu et al. [46] and Hibiki et al. [48], is employed to calculate the distribution of IAC. The conservation equation is:

$$\nabla \cdot \left(\alpha_{\mathrm{g}} \rho_{\mathrm{g}} a \vec{u}_{\mathrm{g}}\right) = \alpha_{\mathrm{g}} \rho_{\mathrm{g}} (S_{\mathrm{RC}} + S_{\mathrm{WE}} + S_{\mathrm{TI}}) - \alpha_{\mathrm{g}} \rho_{\mathrm{g}} a \nabla \vec{u}_{\mathrm{g}} \tag{3.4}$$

where S_{RC}, S_{WE}, and S_{TI} are the terms of bubble coalescence induced by random collision, bubble coalescence induced by wake-entrainment and bubble breakup induced by turbulent impact, respectively.

3.1.4. Species transport

The species transport equation, which is used to compute the transient distribution of impurity in phase 'q', is as follows:

$$\frac{\partial}{\partial t}\left(\alpha_q \rho_q Y_{i,q}\right) + \nabla \cdot \left(\alpha_q \rho_q Y_{i,q} \vec{u}_q\right) = -\nabla \cdot \left(\alpha_q \vec{J}_{i,q}\right) + S_{i,q} \tag{3.5a}$$

where the subscript 'i' denotes [X] or X_2 depending on the phase in question. $Y_{i,q}$ and $\vec{J}_{i,q}$ are the species mass fraction and diffusive flux. The source term $S_{i,q}$ for each phase has the following relation as a result of mass conservation:

$$S_{[X],l} = -S_{X_2,g} \tag{3.5b}$$

For dehydrogenation, the source term is expressed as:

$$S_{[H],l} = \kappa_{[H]} a \rho_l \left(Y_{H,e} - Y_H\right) \tag{3.5c}$$

where κ, a and Y_H are the mass transfer coefficient in liquid, interfacial area concentration, local hydrogen concentration in the computational cell, respectively.

For denitrogenation, the overall rate is decided by the mass transfer in liquid steel and chemical reaction at the interface. The source term is therefore related to the mass transfer rate, J^m, and the chemical reaction rate, J^r:

$$J^m = \frac{A_{l-g} \cdot \kappa_{[N]} \cdot \rho_l}{M_N} \left(Y_{[N],in} - Y_{[N],l}\right) \tag{3.5d}$$

and

$$J^r = \frac{100 \cdot A_{l-g} \cdot k'_N \cdot \rho_l}{M_N} \left(Y^2_{[N],e} - Y^2_{[N],in}\right) \tag{3.5e}$$

where $A_{l\text{-}g}$, M_N, $Y_{[N],in}$, are the interfacial area between steel and gas, mole mass of nitrogen and nitrogen content at the interface, respectively. The apparent chemical reaction rate constant reads:

$$k'_N = \frac{0.15 f_N^2}{(1 + 16100 f_O Y_O + 6340 f_S Y_S)^2} \tag{3.5f}$$

where f_o, f_s, Y_o and Y_s are the activity coefficients and contents of oxygen and sulfur in liquid steel, respectively.

For the mass transfer coefficient in liquid, both Higbie and eddy-cell expressions have been evaluated in the thesis work and the eddy-cell expression appears more accurate in terms of predicting the final hydrogen content in an industrial vacuum tank degasser (VTD). The eddy-cell expression utilized is:

$$\kappa = 0.3\left(D\sqrt{\frac{\varepsilon}{\nu}}\right)^{1/2} \tag{3.5g}$$

where D, ε and ν are the diffusivity in liquid steel, turbulent dissipation rate and kinematic viscosity, respectively.

3.1.5. In-house activity coefficient sub-model

The activity coefficient of dissolved elements in liquid steel has been commonly calculated using the assessed activity data of the liquid phase based on the WLE formalism [74]. In this thesis, however, it is calculated from the liquid phase substitutional solution data of the IAD database [75], which provides thermodynamic data for iron based alloys with solutes Al, C, Cr, H, Mn, N, Nb, Ni, O, P, S, Si, Ti and V. As the substitutional formalism applies mole fractions and expresses solute activities with regard to the Raoultian standard state (pure component) and the WLE formalism applies mass fractions and expresses solute activities with regard to the 1 wt % standard state, the former data must be converted to the latter to obtain the activity coefficient. This is realized by the following formula based on the theory of thermodynamic standard states, as reviewed by Miettinen [76]:

$$f_{\mathrm{X}} = \exp\left(\frac{\mu_{\mathrm{X}}^{\mathrm{L}}}{RT}\right)\frac{M_{\mathrm{X}}}{M_{\mathrm{Fe}}\gamma_{\mathrm{X}}^{\infty\mathrm{L}}Y_{\mathrm{X,e}}} \tag{3.6}$$

where R is the gas constant (8.3145 J/K·mol), M_{X} is the molar weight (g/mol) and M_{Fe} is the molar weight of iron (55.85 g/mol). $\mu_{\mathrm{X}}^{\mathrm{L}}$ is the chemical potential and $\gamma_{\mathrm{X}}^{\infty\mathrm{L}}$ is the activity coefficient of component X in its infinite dilution (solute mole fractions close to zero). Both terms are calculated with the substitutional solution model and data.

3.2. Boundary Conditions

Boundary conditions used in the CFD model are briefly summarized in **Table 3.2**. The surface of liquid bath is considered flat and only gas can escape through the (free) surface. This is realized by adding a set of sink terms into the conservation equations of gas phase in each control volume adjacent to the surface [37]. The sink terms are given as Eqn. (3.7),where w_{g}, A_{fs} and V_{cv} are the gas velocity perpendicular to the free surface, free surface area and volume of numerical grid (control volume), respectively. The gas phase enters calculation domain through a porous nozzle and its velocity is calculated by using Eqn. (3.8), where Q and $A_{\mathrm{nozzle,\,eff}}$ are the gas flow rate and effective area of porous nozzle. The no-slip condition is applied for the liquid, while the slip condition is imposed for the gas at the walls. In addition, the standard wall function is employed for calculating near-wall turbulence quantities.

Table 3.2 Boundary conditions used in the model

Bath surface	Gas inlet	Wall
Degassing boundary $S_\varphi = -\varphi\alpha_g\rho_g\max(w_g, 0)\frac{A_{fs}}{V_{cv}}$ where $\varphi = 1, \vec{u}, k, \varepsilon, Y_i$ Equation (3.7)	Velocity inlet $u_{g,inlet} = \frac{Q}{A_{nozzle,eff}}$ Equation (3.8)	For liquid phase: no-slip condition For gas phase: slip condition For turbulence quantities: standard wall function

3.3. Industrial VTDs

During the thesis work the following three industrial VTDs from different steelmaking plants have been studied: Riva Caronno Works of Italy, VoestAlpine Stahl Donawitz GmbH (VASD) of Austria and Ruukki Metals Oy of Finland. The main dimensions and operating parameters of these VTDs are briefly outlined below.

The structure of the Riva VTD is depicted in **Figure 3.2**, where a porous plug is located at 0.695 m from the center of the bottom. Other dimensions are also shown in the figure.

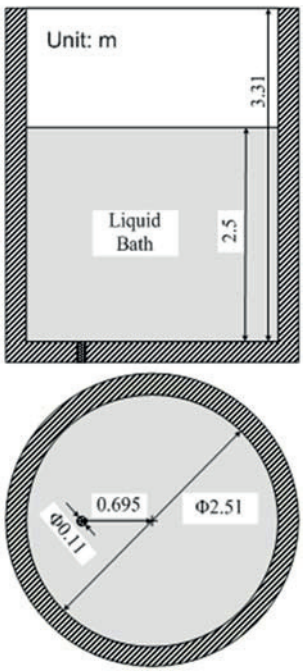

Figure 3.2 Schematic structure of the Riva VTD

The evolution of operating pressure during vacuum treatment in the Riva VTD is illustrated in **Figure 3.3**, where the pressure is lowered rapidly and then reaches a stable condition of deep vacuum (typically under 1.33 mbar), which will last for the remaining period. In addition, argon gas with a high flow rate of 0.15 Nm^3/min is injected at the beginning (lasting about 1 minute) of the deep vacuum condition to create the open-eye. After that, the gas flow rate is reduced to 0.05 Nm^3/min, which is relatively low when compared to many other steel plants. During the entire 25-

minute treatment, the temperature varies from 1913 K (1640 ˚C) to 1868 K (1595 ˚C) and the hydrogen content in liquid steel is reduced from 6.1 ppm to 1.7 ppm.

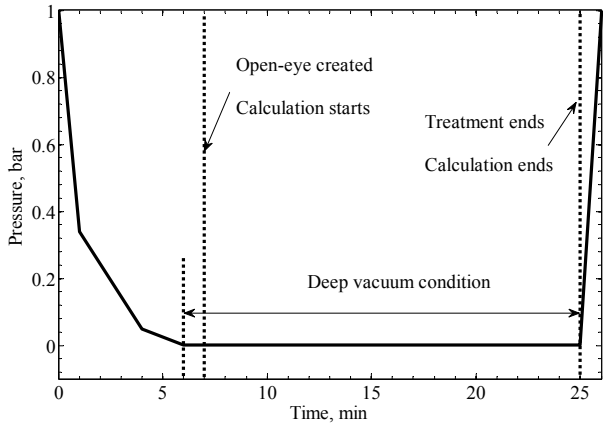

Figure 3.3 Evolution of operating pressure during vacuum treatment in the Riva VTD

Dimensions of the VASD ladle are shown in **Figure 3.4(a)**. The operation pressure is typically below 1-3 mbar and the initial hydrogen content in the liquid steel is 3-4 ppm. The vacuum pressure is reduced rapidly and reaches a stable deep vacuum condition, which lasts about 17 minutes. An argon gas injection rate of 100 NL/min is usually applied in the plant.

A VTD with a capacity of 105-ton liquid steel from Ruukki Metals in Finland is also simulated in this work. During vacuum treatment, nitrogen and hydrogen are simultaneously removed from the VTD. The main dimensions and structure of the ladle are depicted in **Figure 3.4(b)**. Argon gas is injected from two porous plugs eccentrically located at the ladle bottom to provide circulation flow in the liquid bath. The argon flow rate is set so it is approximately equal for each plug and the evolutions of flow rate and operating pressure during vacuum treatment are shown in **Figure 3.5**. As can be seen, the operating pressure is suddenly reduced at the beginning of the treatment and gas flow rate is kept at low level to prevent slag foaming. The flow rate is gradually increased and kept constant as deep vacuum condition (usually below 1 mbar) is achieved in the middle of the process, which lasts about 20 minutes (marked as deep vacuum treatment in the figure).

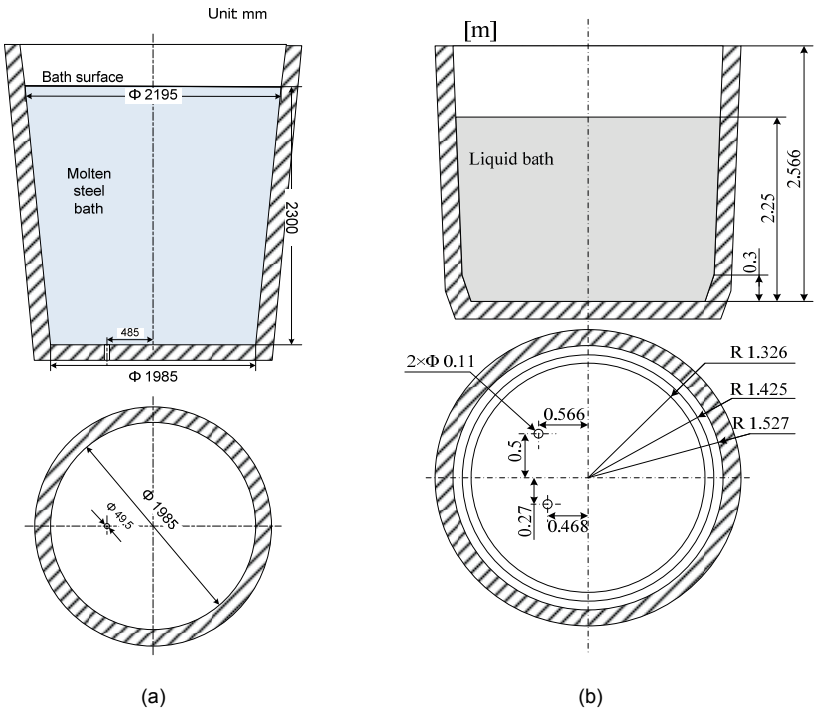

Figure 3.4 (a) Schematic structure of the VASD VTD (b) Schematic structure of the Ruukki VTD

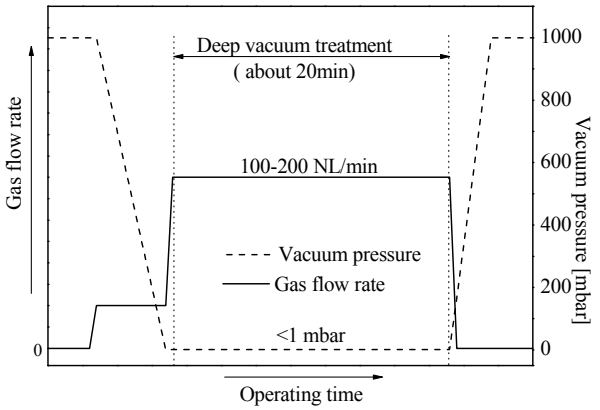

Figure 3.5 Evolutions of operating pressure and gas flow rate during vacuum treatment in the Ruukki VTD

3.4. Results and Discussions

3.4.1. Validation of the multiphase flow model

Figure 3.1 indicates the importance of multiphase flow conditions in the overall predictions. However, to the best of the present author's knowledge, there exist no practical ways to measure the gas-liquid flow within an industrial VTD. Therefore, the multiphase flow sub-model is firstly evaluated on the basis of the experimental study by Sheng and Irons [9, 10]. The comparisons of main parameters between their ex-

perimental set-up and the Riva VTD are listed in **Table 3.3**, where the porous plug size of the Riva ladle is converted to the hydraulic diameter.

Table 3.3 Comparisons of main parameters between the physical model and the Riva ladle

	Physical model by Sheng and Irons [9, 10]	**Riva ladle**
Vessel diameter (m)	0.5	2.51
Nozzle hydraulic diameter (mm)	4.0	5.7
Bath height (m)	0.42	2.5
Liquid density (kg/m^3)	998	7100
Liquid viscosity (Pa·s)	0.001	0.005
Gas density (kg/m^3)	1.225	0.48*
Gas viscosity (Pa·s)×10^5	1.79	8.4*
Gas flow rate (m^3/s)×10^3	0.05-0.15	3.0-6.0*
Fr_{md} (-)	0.068-0.21	0.20-0.40

('*' stands for the properties of argon at temperature of 1873 K (1600 ˚C), pressure of 1.7×10^5 Pa)

It is found that the modified Froude numbers, Fr_{md}, are quite close between the two systems. This implies that, according to the similarity laws, the physical measurements can represent the flow conditions in the Riva VTD to a great extent.

$$\mathrm{Fr_{md}} = \frac{4Q}{\pi d_{\mathrm{hyc}}^2} \frac{1}{\sqrt{|\vec{g}|H}} \sqrt{\frac{\rho_{\mathrm{g}}}{\rho_{\mathrm{l}} - \rho_{\mathrm{g}}}} \tag{3.9}$$

where Q, d_{hyc} and H are the gas flow rate, nozzle hydraulic diameter and bath height, respectively.

The comparisons between the measured and calculated flow fields under different gas flow rates (i.e., 5.0×10^{-5} and 1.5×10^{-4} Nm^3/s) are shown in **Figure 3.6**, where the numerical predictions with standard k-ε equations are also given. In general, the circulating flows, which are located at the upper part of the bath, occur as a main feature in both systems and the liquid flows upwards in the central region as a result of gas injection. The flow direction tilts gradually and is directed to the ladle sidewall near the bath surface and finally, the liquid flows downwards along the sidewall when it becomes far enough away from the intensive injection zone. It is to be noted that the extended turbulent equations could give more accurate predictions in terms of velocity magnitude and the center position of the liquid vortex (*cf.* the red dot in the figure).

For detailed information, the measured and calculated axial liquid velocities along the center line are plotted in **Figure 3.7**. Based on the five measured points, the average deviations of the calculated values with extended turbulence equations are about 6 % and 13 % for the cases with low and high gas flow rate, respectively. However, the deviations with standard turbulence equations are approximately 30 % for both cases. Therefore, the calculated results using the extended turbulence equations are more accurate when compared to the experimental data.

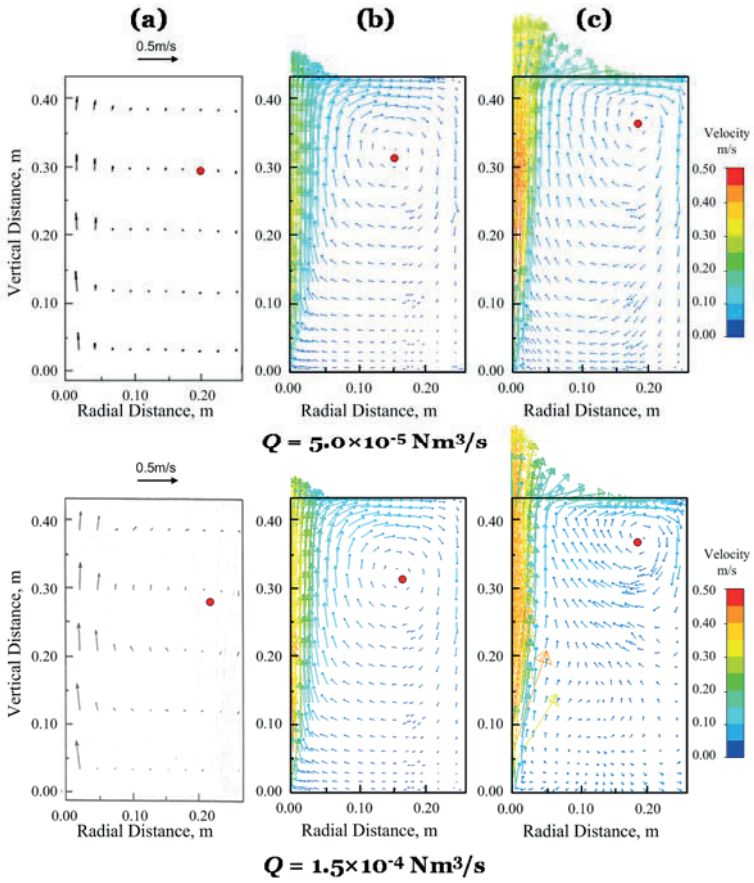

Figure 3.6 Comparisons of flow fields between physical and numerical results under different gas flow rates: (a) Experimental measurements, (b) Predictions with the extended turbulence equations, (c) Predictions with standard turbulence equations

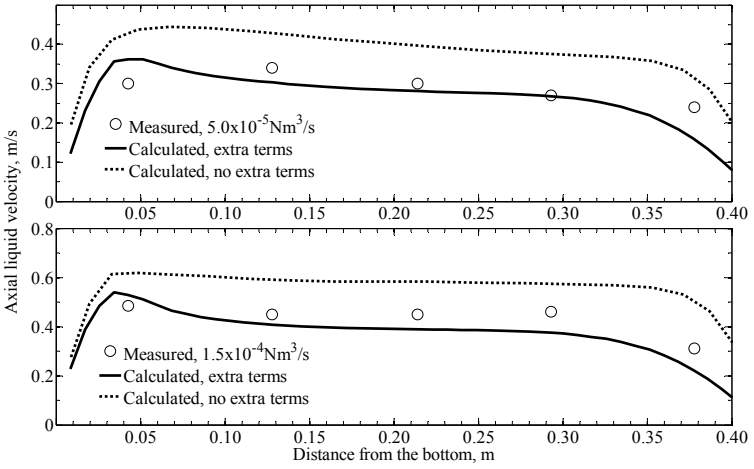

Figure 3.7 Comparisons of axial liquid velocity between physical and numerical results under different gas flow rates

Similarly, the comparisons between the measured and calculated TKE under different gas flow rates are depicted in **Figure 3.8**, and the detailed comparisons of TKE along the center line are plotted in **Figure 3.9**. It is found that by using the extended turbulence equations the deviations from the measured points are 18 % and 7 % for the two cases, which are much lower than the ones (about 85 %) with the standard equations. This suggests that the accuracy of prediction can be improved by using the extended turbulence equations even though it shows some deviations of TKE near the vessel bottom and bath surface (*cf.* **Figure 3.8** and **Figure 3.9**). This could be explained by the nature of the k-ε equations that are known to overestimate turbulence quantities especially in strongly curved flows. Nevertheless, the developed multiphase sub-model in this work appears accurate enough to investigate the complex flow behavior in the industrial vacuum degasser.

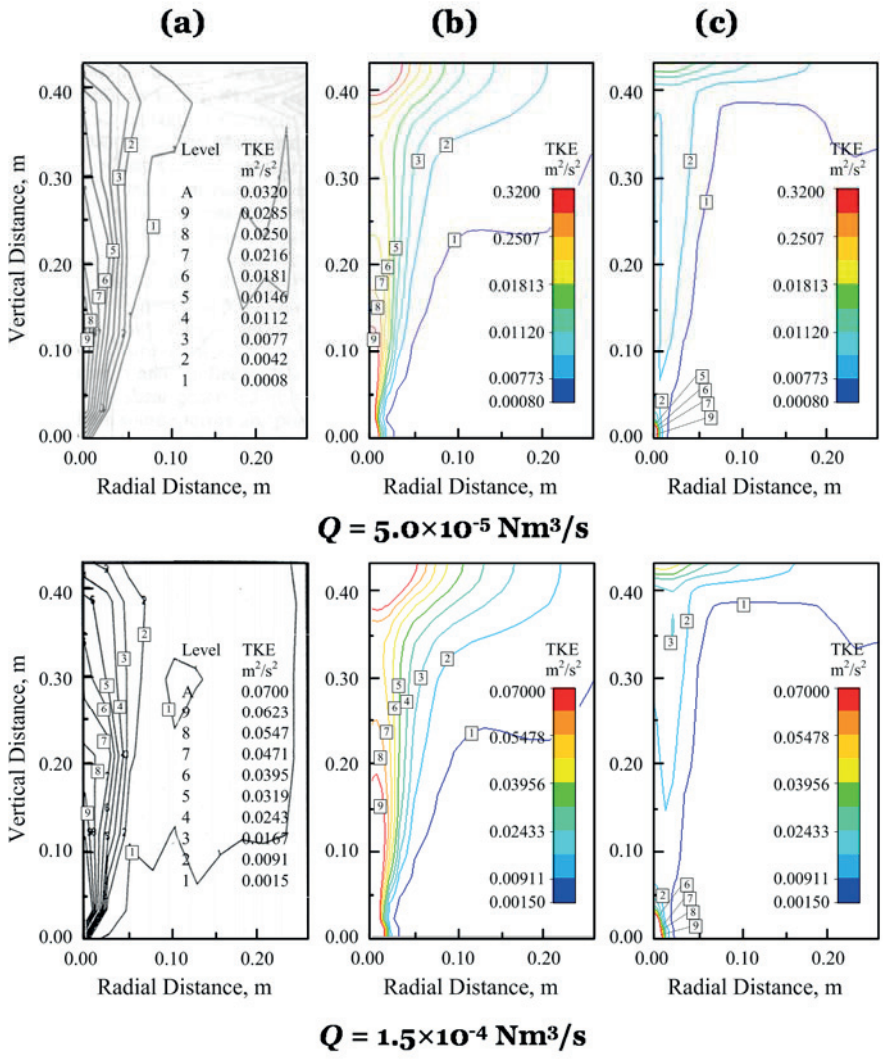

Figure 3.8 Comparisons of TKE between physical and numerical results under different gas flow rates: (a) Experimental measurements, (b) Predictions with the extended turbulence equations, (c) Predictions with standard turbulence equations

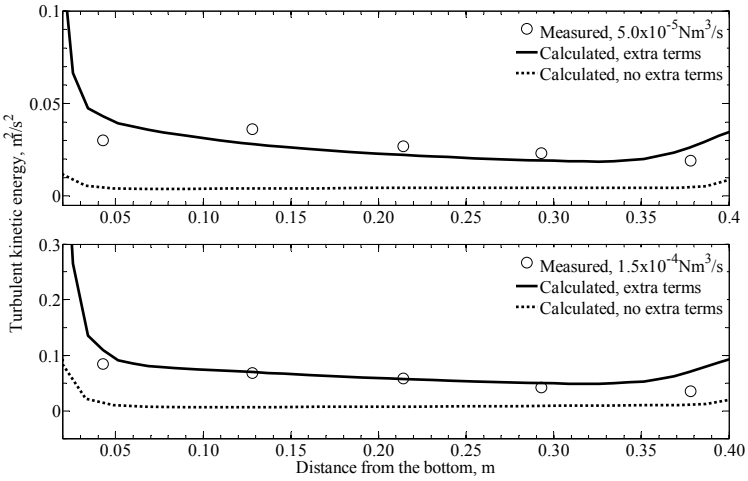

Figure 3.9 Comparisons of TKE between physical and numerical results under different gas flow rates

3.4.2. Simulations of hydrogen removal

The CFD model is adopted to simulate the dehydrogenation process both in the Riva and the VASD degasser. Only the deep vacuum period of each VTD is considered and the overlaying slag phase is ignored in the simulations. The general assumptions, simplifications and boundary conditions for each industrial case can be found in **Paper I-III** (*cf.* Appendix).

3.4.2.1. Riva cases

To study the effect of vacuum pressure on hydrogen removal, three cases with different vacuum pressures (P_v) are simulated: 1 mbar for Case 1; 2 mbar for Case 2; 10 mbar for Case 3. In addition, the initial hydrogen content in liquid steel ([H]) and gas flow rate of 6.1 ppm and 0.05 Nm^3/min are the same for the three cases. It should be noted here that Case 1 corresponds to one of the practical operation conditions in the plant (i.e., Riva Caronno Works of Italy). The hydrogen transport equations are solved based on the stationary flow field obtained with the multiphase sub-model and some detailed results are displayed in **Figure 3.10**.

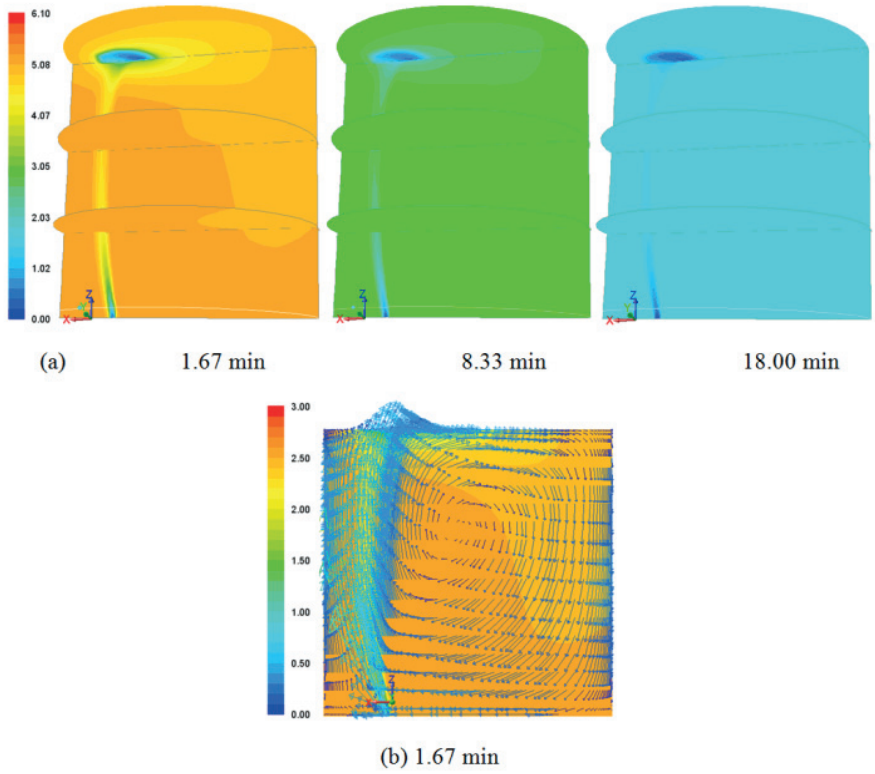

Figure 3.10 Some detailed calculated results for Case 1: (a) Transient distribution of [H] (in ppm); (b) Hydrogen content as well as velocity field (in m/s) in the central plane

As is clear from the figure, [H] decreases during the vacuum treatment and a low [H] zone appears both in the gas plume and bath surface. This can be explained by the locally low hydrogen partial pressure in the bubbles and at the surface. Also, it can be seen that [H] is higher in the regions that are remote from the gas plume and open-eye.

In principle, hydrogen removal could take place through the bubble surface and bath surface. These two routes are compared in **Figure 3.11**, where the evolutions of dehydrogenation rate by gas bubbles and by bath surface are plotted. It is shown that the bubble surface is the main area for hydrogen removal especially at the beginning of the process. As can be seen in the figure, dehydrogenation rate on bubble surface is 5 times higher as the process commences since the gas-liquid interfacial area is much higher than that at the bath surface. The dehydrogenation rates for both routes decrease during the process due to the descent of [H] in the bath, leading to the decay of the driving force for mass transfer, *i.e.* the concentration gradient. However, the dehydrogenation rate at the bath surface does not decrease as much as the one for gas bubbles. This could also be explained by the driving force: the hydrogen content around the open-eye is always at a lower level when compared to the one in the bulk flow (*cf.* **Figure 3.10**), giving rise to a lower driving force for the removal reaction at the bath surface.

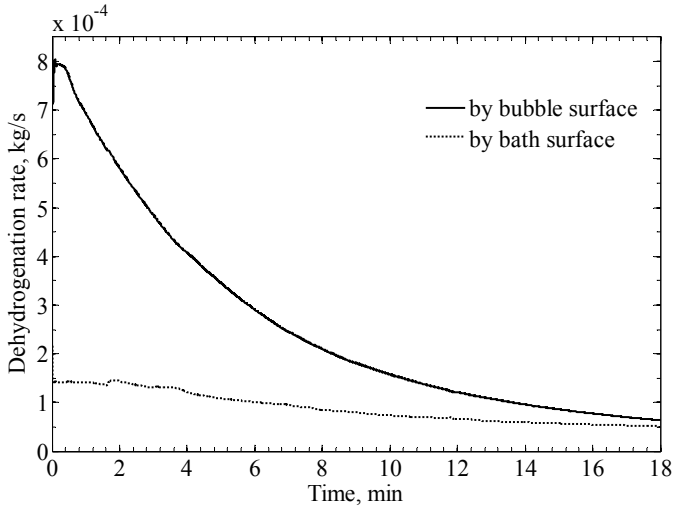

Figure 3.11 Dehydrogenation rates by bubble surface and bath surface for Case 1

The effect of vacuum pressure on dehydrogenation is illustrated in **Figure 3.12**, where the [H] removal ratio for each route, *i.e.* bubble surface or bath surface, is depicted. It can be seen that the total removal ratio decreases when the vacuum pressure increases since the thermodynamic conditions for dehydrogenation in the liquid bath deteriorate with increasing vacuum pressure. Furthermore, as shown in the figure, the removal ratio from the bath surface slightly increases for Case 3 with much higher vacuum pressure. This can be explained as follows: the liquid steel with higher [H] (because of the worse dehydrogenation conditions in the bath) could reach the bath surface where the partial pressure of hydrogen is fixed due to the assumption of zero-H_2 partial pressure. The driving force of dehydrogenation near the bath surface therefore rises, causing the higher removal ratio at the bath surface.

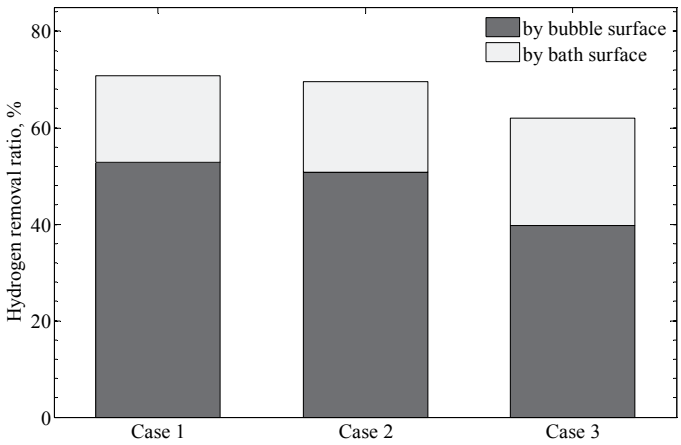

Figure 3.12 Effect of vacuum pressure on hydrogen removal ratio for Cases 1-3

In order to validate the integrated model, three more cases, which correspond to operating conditions in the plant and are listed in **Table 3.4**, were performed. The calculated final [H] for Case 4-6 as well as that of Case 1 are plotted in **Figure 3.13**,

where the measured data from the plant are also given. As can be seen, the biggest deviation of 6.2% occurs with Case 4, a good agreement is still achieved between prediction and measurement.

Table 3.4 Main parameters for Cases 4-6 of Riva VTD

	Case 4	**Case 5**	**Case 6**
Vacuum pressure, mbar	0.72	0.78	0.58
Gas flow rate, Nm^3/min	0.07	0.08	0.1
Deep vacuum period, min	21	15	20
Initial [H], ppm	5.9	5.6	5.8

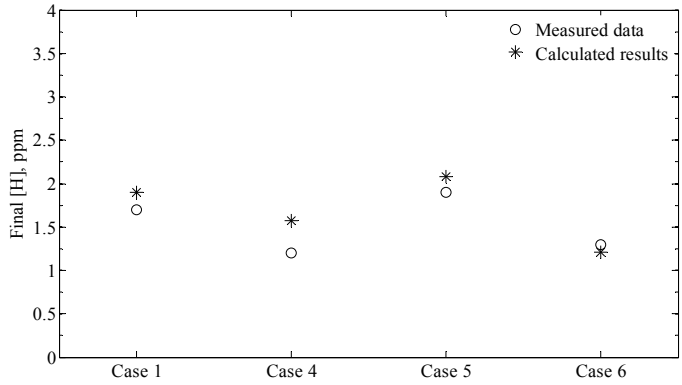

Figure 3.13 Comparisons of measured and calculated final hydrogen content in liquid steel

3.4.2.2. *VASD cases*

For the VASD ladle, the transient distributions of [H] during the treatment as well as the velocity field on the center plane are illustrated in **Figure 3.14**. This shows similar patterns to **Figure 3.10**: [H] decreases during the process and low [H] zones appear near the gas plume and open-eye.

Figure 3.15 shows the evolutions of [H] in liquid steel with different initial [H]. As can be seen, [H] in liquid steel decreases during the process and more interestingly, the effect of initial [H] on the final content seems to be minor when the vacuum time is long enough, e.g. only a difference of 0.085 ppm exists among the three cases with 17-min of deep vacuum. In addition, since measurements of [H] in the degasser are unavailable from this particular plant set-up, a set of average data based on the measurements from various tundish heats with liquid steel after different durations of vacuum treatment (*cf.* 8-17 minutes in the figure) are given for comparison. It is shown that the simulation results differ up to 6% from the average data, indicating that the predicted curves correspond well with the average data. This could verify the CFD model if the tundish data can reflect the final [H] in the VTD to a great extent, which in fact has been confirmed by the personnel from the plant (*i.e.* VoestAlpine Stahl Donawitz GmbH of Austria).

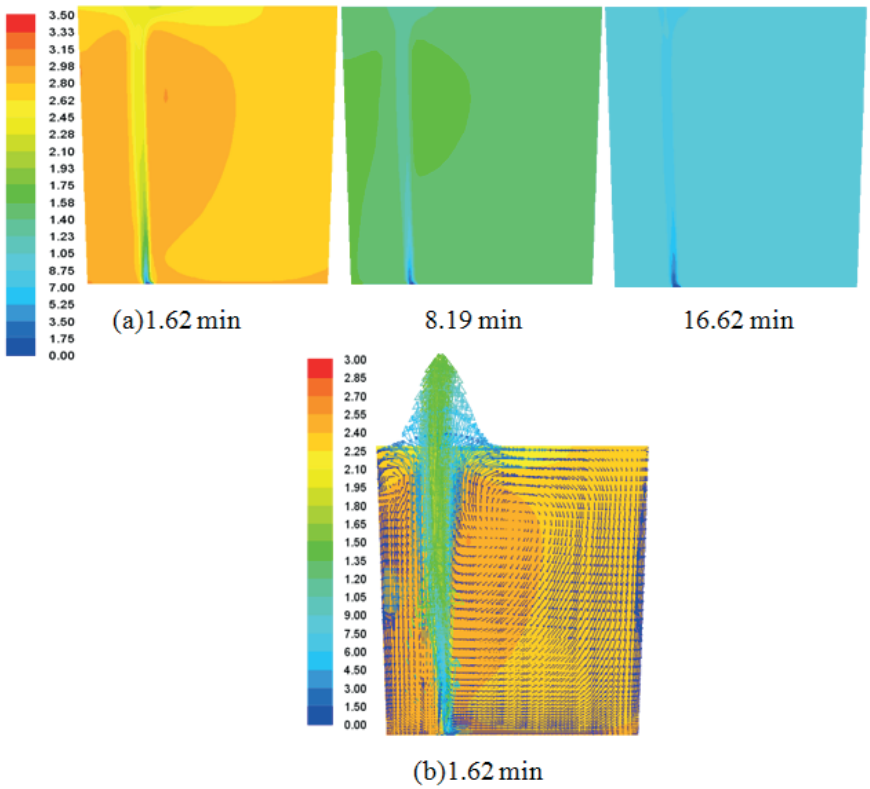

Figure 3.14 (a) Transient distribution of [H] in the steel bath ([H] in ppm) (b) Hydrogen content with the corresponding velocity field (in m/s) on the center plane for a VASD case (initial [H] is 3.5 ppm)

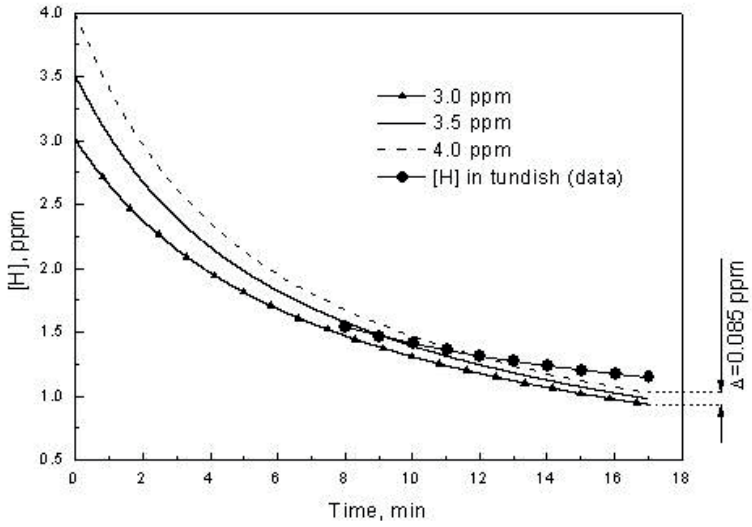

Figure 3.15 Evolutions of hydrogen content in liquid steel with different initial [H] for the VASD ladle

3.4.3. Simulations of hydrogen and nitrogen removal (Ruukki cases)

The process of simultaneous dehydrogenation and denitrogenation in the Ruukki degasser is simulated by using the integrated model. The variation in the steel composition before the degassing operation is listed in **Table 3.5**. It is worth noting that the carbon content is in the range of 0.1% to 0.35% and the oxygen content is generally lower than 6 ppm, which implies that decarburization could barely take place in the VTD.

Table 3.5 Variation in Ruukki steel composition before degassing treatment

	Al	C	Cr	H	Mn	N	Nb
Min.	0.015	0.1	0.033	0.0004*	0.6	0.003	0
Max.	0.127	0.35	1.78	0.0004*	1.4	0.0073	0.081
	Ni	**O**	**P**	**S**	**Si**	**Ti**	**V**
Min.	0.03	0.0002	0.006	0.0016	0.09	0.002	0.005
Max.	0.66	0.0006	0.017	0.0154	0.5	0.126	0.198

(* stands for average content in liquid steel)

Figure 3.16 illustrates the evolution of nitrogen and hydrogen contents in liquid steel during deep vacuum treatment for a base case of the Ruukki ladle. As can be seen, the contents of nitrogen and hydrogen gradually decrease as the operation proceeds and the low content zones appear in the vicinity of the plume.

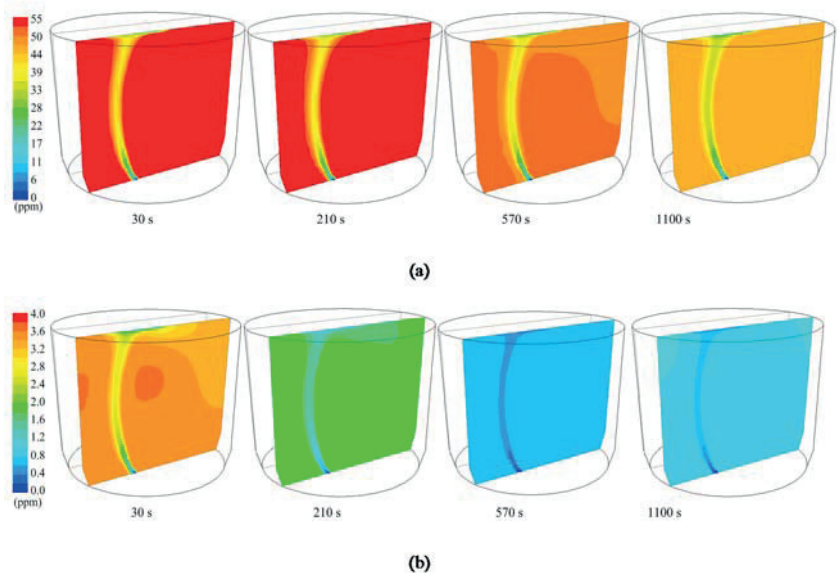

Figure 3.16 Transient distribution of (a) nitrogen and (b) hydrogen in liquid steel during deep vacuum treatment for the Ruukki ladle

3.4.3.1. Effect of alloying agent on denitrogenation

The effect of various alloying agents on the denitrogenation process is estimated by conducting simulations with different contents of each alloying element. The evolutions of the apparent chemical reaction rate under different alloying element contents are displayed in **Figure 3.17**, where the average rate over the 19-min deep vacuum

period is plotted and the content range of each element is chosen according to **Table 3.5**. As can be seen in **Figure 3.17 (a)**, the reaction rate decreases with an increase in the content of [S] or [O], because sulfur or oxygen as a surface-active element can block the interfacial reaction sites and consequently retard the chemical reaction rate. Furthermore, the reaction rate decreases as each of [Cr], [Nb], [V], [Ti] or [Mn] content increases (*cf*. **Figure 3.17 (a)**) since those elements have stronger affinity with nitrogen than iron, therefore lowering the nitrogen activity in liquid steel and reducing the reaction rate. In contrast, as demonstrated in **Figure 3.17 (b)**, an increase in the content of [C], [Si], [P] or [Ni] can promote the reaction rate as these elements have stronger repulsive force against nitrogen than iron and thus increase the nitrogen activity. In addition, the presence of aluminum slightly enhances the nitrogen reaction rate even though it has stronger affinity with nitrogen than iron.

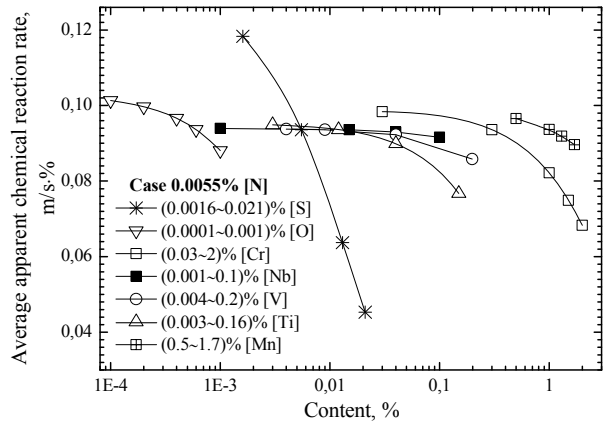

(a)

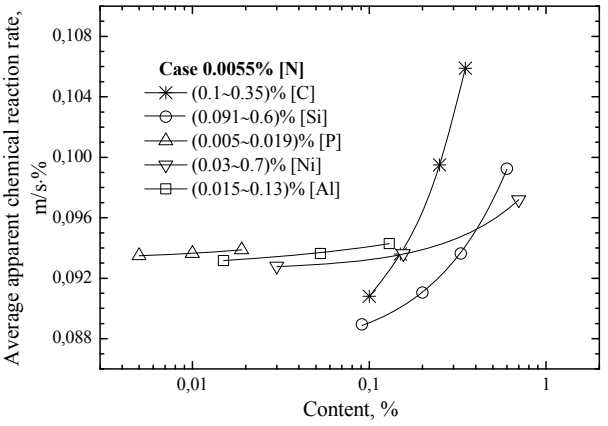

(b)

Figure 3.17 Effect of various alloying elements on the (average) apparent chemical reaction rate

The effects mentioned above are further elucidated in **Table 3.6**, where the influence of each alloying element on the activity coefficients and chemical reaction rate is listed. In principle, the influence of an element on nitrogen reaction rate is attributed

not only to its effect on the activity of nitrogen in liquid steel but it is also linked to its influence on the activities of sulfur and oxygen, which are at the same time determined by the other alloying elements present in the liquid steel. This is reflected in the last column of **Table 3.6**: Even though an increase in [Al] content reduces the activity of nitrogen, it leads to an increase in the sulfur activity and lowers the activity of oxygen. Consequently, its effect on the chemical reaction rate is a combination of all those aspects. It should be noted that although the presented results are valid for the steel composition studied here, the developed concept is general and would be applicable for other steel grades.

Table 3.6 Effect of various alloying elements on the activity coefficients and chemical reaction rate

	Cr	Nb	V	Ti	Mn	C	Si	P	Ni	Al
f_N	−	−	−	−	−	+	+	+	+	−
f_S	−	−	−	−	−	+	+	+	+	+
f_O	−	−	−	−	−	−	−	−	+	−
k_N	−	−	−	−	−	+	+	+	+	+

3.4.3.2. Operating diagram of denitrogenation for on-line use

Emphasis behind the present work has also been put into clarifying the correlations between the chemical reaction rate (constant), initial and final [N] content and thus providing the managers and operators with some instructive information in real-time. To this end, a diagram of final [N] content and nitrogen removal ratio can be plotted on the basis of extensive numerical experiments with various operating parameters using the integrated CFD model.

Figure 3.18 illustrates two operating diagrams under different gas flow rates. It must be stressed that all the simulations behind the figures are performed for 1100 seconds corresponding to the deep vacuum period of the degassing process and the liquid steel composition varies in each simulation to cover the whole range of the steel composition listed in **Table 3.5**. It is generally concluded from the figures that the final [N] content decreases with an increase in the average reaction rate constant and increases as the initial content rises. The nitrogen removal ratio, which is defined as the removed nitrogen in liquid steel relative to the initial one, is marked with dashed lines. It shows that the removal ratio rises as either the rate constant or the initial [N] content increases. In addition, by comparing **Figure 3.18 (a)** and **(b)**, it can be seen that each line of the removal ratio moves downwards with higher gas flow rate, indicating that more nitrogen can be removed from liquid steel when the bath is more stirred.

The operating diagrams demonstrated above are further verified with some industrial measurements from the plant. Comparisons of measured and predicted final [N] contents under different gas flow rates are shown in **Figure 3.19**, where each predicted content are determined from the operating diagrams with corresponding initial [N] content, gas flow rate and calculated average chemical reaction rate constant based on the steel composition. It is calculated that the average deviations of the predicted results are lower than 13% and 10% for the cases with low and high gas flow rate respectively. This suggests that the operating diagrams presented in this report would be an informative and accurate tool for VTD managers and operators.

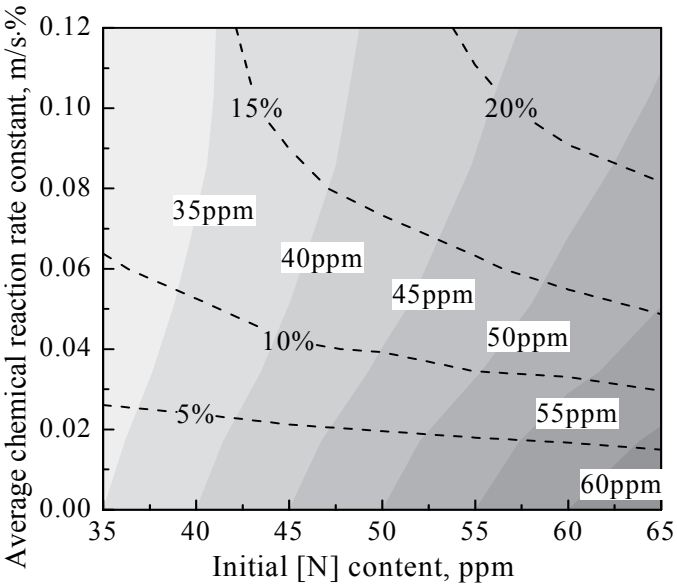

(a)

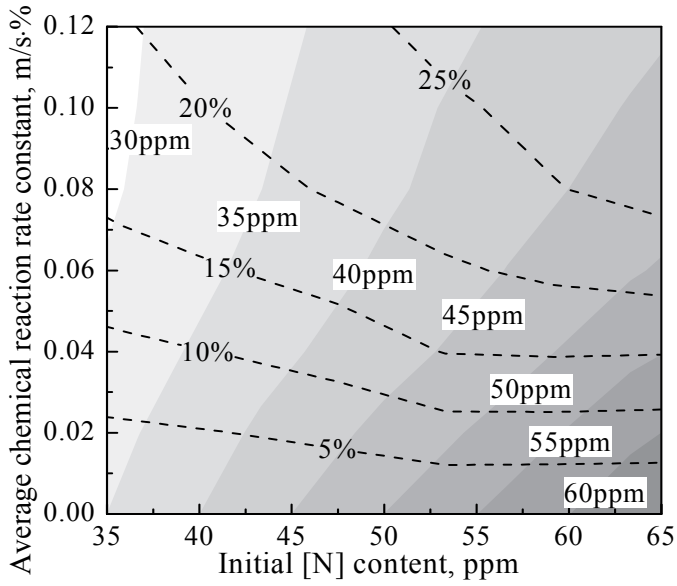

(b)

Figure 3.18 Operating diagrams based on predictions of the CFD model: (a) gas flow rate of 130 NL/min and (b) of 180 NL/min per plug. The nitrogen removal ratio is marked with dashed lines

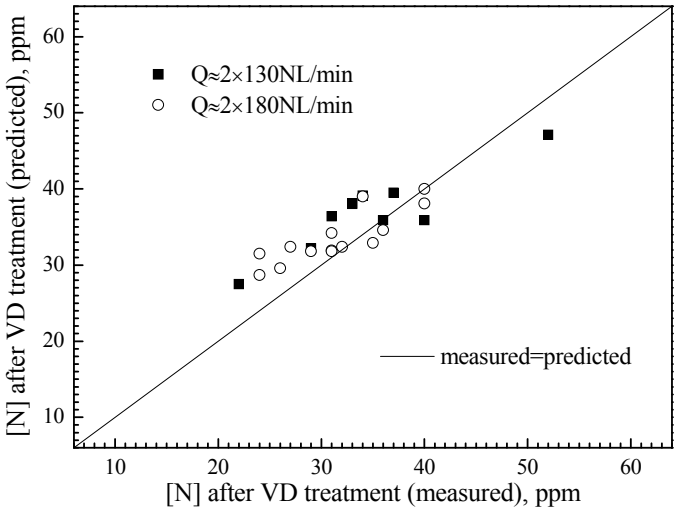

Figure 3.19 Comparisons of measured data of final [N] and the ones by corresponding operating diagrams

4. Conclusions

The CFD technique has been proven to be a powerful tool for simulating various transport phenomena within metallurgical reactors, which are typically operated under extremely hostile conditions. Nevertheless, different thermodynamic constraints should be considered for each specific metallurgical reactor in order to provide a better understanding of the underlying process. This thesis work has placed particular emphasis on investigating the dehydrogenation and/or denitrogenation behavior in some operational VTDs from different industrial plants. To this end, a comprehensive CFD model has been developed step by step during the thesis work, of which the novelties and new features exist in the following aspects.

- A literature survey was firstly conducted in the related field and a variety of elaborate sub-models and concepts, which are relatively separate in the literature, have been integrated into the CFD model.
- The multi-component effect of steel composition on the degassing process has been assessed by coupling the CFD model with an in-house thermodynamics code, which can be used to calculate the activity coefficient of dissolved elements in liquid steel as a function of steel composition and temperature.
- Efforts were put into developing an "*on-line use*" concept to control the nitrogen removal since CFD calculations are often time-consuming and are therefore, so far, inappropriate for on-line use.

The CFD model was developed on the basis of the Eulerian-Eulerian approach and consists of two sub-routines for calculating multiphase flows and species transportations, respectively. The commercial CFD package of ANSYS FLUENT was adopted and augmented by implementing various user-defined functions. The versatility of the model has been demonstrated by performing different simulations to cover a wide range of main operating parameters of the VTDs. Also, the accuracy of the model was established by performing comparisons against industrial measurements. The main findings from this thesis work are summarized as follows.

- The multiphase model with extended turbulent equations gives more accurate results compared to the model with standard turbulent equations. (as in **Paper I**)
- Hydrogen removal takes place both at the bubble-liquid interface and at the bath surface, though the bubble surface was determined to be the main area for dehydrogenation especially at the beginning of the process. (as in **Paper I**)
- The model was applied to study the simultaneous removal of hydrogen and nitrogen in liquid steel and the predicted results indicated that lower hydrogen and nitrogen content can be achieved by increasing the gas flow rate and prolonging the deep vacuum duration. (as in **Paper II**)

- The effect of various alloying elements on denitrogenation process was estimated and the simulations revealed that the nitrogen removal rate decreases with an increase in the content of [S], [O], [Cr], [Nb], [V], [Ti] or [Mn], whereas it increases with an increase in the content of [C], [Si], [P], [Ni] or [Al]. (as in **Paper III**)
- The 3D operating diagrams, which correlate the chemical reaction rate constant and initial nitrogen content to its final content in liquid steel, were presented. It has been shown that these operating diagrams would be a useful tool for providing instructive information to VTD managers and operators. (as in **Paper IV**)

5. Future Prospects

Still, there are a number of issues to be tackled regarding the CFD model. More validation against industrial data from different steel grades will be carried out in the near future. The accuracy of the model will be improved to further reduce the (small) discrepancies between predicted results and industrial measurements by tuning some of the assumptions and/or parameters. The overlaying slag phase will be embodied in the model so that the desulphurization process can be simulated, in order to make the model more versatile and flexible. Moreover, an attempt to performing parallel simulations will also be made.

6. References

1. A. Ghosh. Secondary Steelmaking, Principles and Applications. CRC Press, 2001.
2. D. Mazumdar and J.W. Evans. Modeling of Steelmaking Processes. CRC Press, 2010.
3. T.C. Hsiao, T. Lehner and B. Kjellberg. Fluid Flow in Ladles-Experimental Results. Scandinavian Journal of Metallurgy, Vol.9 (1980), pp. 105-110.
4. J. Szekely, H.J. Wang and K.M. Kiser. Flow Pattern Velocity and Turbulence Energy Measurements and Predictions in a Water Model of an Argon-stirred Ladle. Metallurgical Transactions B, Vol. 7 (1976), pp. 287-295.
5. J.H. Grevet, J. Szekely and N. El-Kaddah. An Experimental and Theoretical Study of Gas Bubble Driven Circulation Systems. International Journal of Heat and Mass Transfer, Vol. 25 (1982), pp. 487-497.
6. A.H. Castillejos and J.K. Brimacombe. Measurement of Physical Characteristics of Bubbles in Gas-liquid Plumes: Part II. Local Properties of Turbulent Air-water Plumes in Vertically Injected Jets. Metallurgical Transactions B, Vol. 18 (1987), pp. 659-671.
7. G.G. Krishna-Murthy, A. Ghosh and S.P. Mehrotra. Characterization of Two-phase Axisymmetric Plume in a Gas Stirred Liquid Bath—A Water Model Study. Metallurgical Transactions B, Vol. 19 (1988), pp. 885-892.
8. P.E. Anagbo, J.K. Brimacombe and A.H. Castillejos. A Unified Representation of Gas Dispersion in Upwardly Injected Submerged Gas Jets. Canadian Metallurgical Quarterly, Vol. 28 (1989), pp. 323-330.
9. Y.Y. Sheng and G.A. Irons. Measurements of the Internal Structure of Gas-liquid Plumes. Metallurgical Transactions B, Vol. 23 (1992), pp. 779-788.
10. Y.Y. Sheng and G.A. Irons. Measurement and Modeling of Turbulence in the Gas/Liquid Two-Phase Zone during Gas Injection. Metallurgical Transactions B, Vol. 24 (1993), pp. 695-705.
11. S.T. Johansen, D.G.C. Robertson, K. Woje and T.A. Engh. Fluid Dynamics in Bubble Stirred Ladles: Part I. Experiments. Metallurgical Transactions B, Vol. 19 (1988), pp. 745-754.
12. Y. Sahai and R.I.L. Guthrie. Hydrodynamics of Gas Stirred Melts: Part I. Gas/Liquid Coupling. Metallurgical Transactions B, Vol. 13 (1982), pp. 193-202.
13. D.Mazumdar and R.I.L. Guthrie. Hydrodynamic Modeling of Some Gas Injection Procedures in Ladle Metallurgy Operations. Metallurgical Transactions B, Vol. 16 (1985), pp. 83-90.
14. D.Mazumdar, R.I.L. Guthrie and Y. Sahai. On Mathematical Models and Numerical Solutions of Gas Stirred Ladle Systems. Applied Mathematical Modeling, Vol. 17 (1993), pp. 255-262.
15. Y. Sahai and R.I.L. Guthrie. Hydrodynamics of Gas Stirred Melts: Part II. Axisymmetric Flows. Metallurgical Transactions B, Vol. 13 (1982), pp. 203-211.
16. D.Mazumdar and R.I.L. Guthrie. Mixing Models for Gas Stirred Metallurgy Reactors. Metallurgical Transactions B, Vol. 17 (1986), pp. 725-733.
17. J. Szekely, A.H. Dilawari and R. Metz. The Mathematical and Physical Modeling of Turbulent Recirculating Flows. Metallurgical Transactions B, Vol. 10 (1979), pp. 33-41.

18. T. Deb Roy, A.K. Majumdar and D.B. Spalding. Numerical Prediction of Recirculation Flows with Free Convection encountered in Gas-agitated Reactors. Applied Mathematical Modelling, Vol. 2 (1978), pp. 146-150.
19. A.H. Castillejos M.E. Salcudean and J.K. Brimacombe. Fluid Flow and Bath Temperature Destratification in Gas-stirred Ladles. Metallurgical Transactions B, Vol. 20 (1989), pp. 603-611.
20. M.Y. Zhu, I. Sawada, N. Yamasaki and T.C. Hsiao. Numerical Simulation of Three-dimensional Fluid Flow and Mixing Process in Gas-stirred Ladles. ISIJ International, Vol. 36 (1996), pp. 503-511.
21. S.T. Johansen and F. Boysan. Fluid Dynamics in Bubble Stirred Ladles: Part II. Mathematical Modeling. Metallurgical Transactions B, Vol. 19 (1988), pp. 755-764.
22. D. Mazumdar and R.I.L. Guthrie. An Assessment of a Two Phase Calculation Procedure for Hydrodynamic Modelling of Submerged Gas Injection in Ladles. ISIJ International, Vol. 34 (1994), pp. 384-392.
23. D. Guo and G.A. Irons. Modeling of Gas-liquid Reactions in Ladle Metallurgy: Part II. Numerical Simulation. Metallurgical Transactions B, Vol. 31 (2000), pp. 1457-1464.
24. Y. Xie, S. Orsten and F. Oeters. Behavior of Bubbles at Gas Blowing into Liquid Wood's Metal. ISIJ International, Vol. 32 (1992), pp. 66-75.
25. Y. Xie and F. Oeters. Measurement of Bubble Plume Behavior and Flow Velocity in Gas Stirred Liquid Wood's Metal with an Eccentric Nozzle Position. Steel Research, Vol. 65 (1994), pp. 315-319.
26. J.E. Olsen and S. Cloete. Coupled DPM and VOF Model for Analyses of Gas Stirred Ladles at Higher Gas Rates. Seventh International Conference on CFD in the Minerals and Process Industries, Melbourne, Australia, 2009.
27. S.W.P. Cloete. A Mathematical Modelling Study of Fluid Flow and Mixing in Gas Stirred Ladles. Master Thesis, Stellenbosch University, 2008.
28. F. Oeters, W. Pluschkell, E. Steinmetz and H. Wilhelmi. Fluid Flow and Mixing in Secondary Metallurgy. Steel Research, Vol. 59 (1988), pp, 192-201.
29. M.P. Schwarz and W.J. Turner. Applicability of the Standard k-ε Turbulence Model to Gas-stirred Baths. Applied Mathematical Modeling, Vol. 12 (1988), pp. 273-279.
30. O.J. Ilegbusi and J. Szekely. The Modelling of Gas-bubble Driven Circulations Systems. ISIJ International, Vol. 30 (1990), pp. 731-739.
31. P. Jönsson and L. Jonsson. A Model of a Gas-stirred Ladle. Scandinavian Journal of Metallurgy, Vol. 24 (1995), pp. 194-206.
32. L. Jonsson and P. Jönsson. Modeling of the Fluid Conditions around the Slag Metal Interface in a Gas-stirred Ladle. ISIJ International, Vol. 36 (1996), pp. 1127-1134.
33. H. Turkoglu and B. Farouk. Mixing Time and Liquid Circulation Rate in Steelmaking Ladles with Vertical Gas Injection. ISIJ International, Vol. 31 (1991), pp. 1371-1380.
34. O.J. Ilegbusi, J. Szekely, M. Iguchi, H. Takeuchi and Z. Morita. A Comparison of Experimentally Measured and Theoretically Calculated Velocity Fields in a Water Model of an Argon Stirred Ladle. ISIJ International, Vol. 33 (1993), pp. 474-478.
35. J.F. Domgin, P. Gardin and M. Brunet. Experimental and Numerical Investigation of Gas Stirred Ladles. Second International Conference on CFD in the Minerals and Process Industries, Melbourne, Australia, 1999.
36. J. Hua and C.H. Wang. Numerical Simulation of Bubble-driven Liquid Flows. Chemical Engineering Science, Vol. 55 (2000), pp. 4159-4173.
37. J.L. Xia, T. Ahokainen and L. Holappa. Analysis of Flows in a Ladle with Gas-stirred Melt. Scandinavian Journal of Metallurgy, Vol. 30 (2001), pp. 69-76.

38. M.L. Bertodano, F.J. Moraga, D.A. Drew and R.T. Lahey. The Modeling of Lift and Dispersion Forces in Two-fluid Model Simulations of a Bubbly Jet. Journal of Fluids Engineering, Vol. 126 (2004), pp. 573-577.
39. S.M. Monahan, V.S. Vitankar and R.O. Fox. CFD Predictions for Flow-regime Transitions in Bubble Columns. AIChE Journal, Vol. 51 (2005), pp. 1897-1923.
40. C.G. Mendez, N. Nigro and A. Cardona. Drag and Non-drag force Influences in Numerical Simulations of Metallurgical Ladles. Journal of Materials Processing Technology, Vol. 160 (2005), pp. 296-305.
41. G. Venturini and M.B. Goldschmit. Gas-liquid Reaction Model in Gas-stirred Systems: Part 1. Numerical Model. Metallurgical Transactions B, Vol. 38 (2007), pp. 461-475.
42. W. Lou and M. Zhu. Numerical Simulation of Gas and Liquid Two-phase Flow in Gas-stirred System Based on Euler-Euler Approach. Metallurgical Transactions B, Vol. 44 (2013), pp. 1251-1263.
43. J.P. Bellot, V. D. Felice, B. Dussoubs, A. Jardy and S. Hans. Coupling of CFD and PBE Calculations to Simulate the Behavior of an Inclusion Population in a Gas-stirred Ladle. Metallurgical Transactions B, Vol. 44 (2013), pp. 1543-1916.
44. G. Kocamustafaogullari and M. Ishii. Interfacial Area and Nucleation Site Density in Boiling Systems. International Journal of Heat and Mass Transfer, Vol. 26 (1983), pp. 1377-1387.
45. G. Kocamustafaogullari and M. Ishii. Foundation of the Interfacial Area Transport Equation and its Closure Relations. International Journal of Heat and Mass Transfer, Vol. 38 (1995), pp. 481-493.
46. Q. Wu, S. Kim and M. Ishii. One-group Interfacial Area Transport in Vertical Bubbly Flow. International Journal of Heat and Mass Transfer, Vol. 41 (1998), pp. 1103-1112.
47. T. Hibiki and M. Ishii. Two-group Interfacial Area Transport Equations at Bubbly-to-slug Flow Transition. Nuclear Engineering and Design, Vol. 202 (2000), pp. 39-76.
48. T. Hibiki and M. Ishii. Development of One-group Interfacial Area Transport Equation in Bubbly Flow Systems. International Journal of Heat and Mass Transfer, Vol. 45 (2002), pp. 2351-2372.
49. M. Ishii, S. Kim and J. Kelly. Development of Interfacial Area Transport Equation. Nuclear Engineering and Technology, Vol. 37 (2005), pp. 525-536.
50. S. Taniguchi, S. Kawaguchi and A. Kikuchi. Fluid Flow and Gas-liquid Mass Transfer in Gas-injected Vessels. Applied Mathematical Modelling, Vol. 26 (2002), pp. 249-262.
51. D. Mazumdar and R.I.L Guthrie. The Physical and Mathematical Modeling of Gas Stirred Ladle Systems. ISIJ International, Vol. 35 (1995), pp. 1-20.
52. S.T. Johansen and F. Boysan. Fluid Dynamics in Bubble Stirred Ladles: Part II. Mathematical Modeling. Metallurgical Transactions B, Vol. 19 (1988), pp. 755-764.
53. L. Jonsson. Mathematical Modeling of Selected Ladle Operations. Doctor Thesis, Royal Institute of Technology (KTH), 1998.
54. A. Jauhiainen, L. Jonsson, P. Jönsson and S. Eriksson. The Influence of Stirring Method on Hydrogen Removal During Ladle Treatment. Steel Research, Vol. 73 (2002), pp. 82-90.
55. M. Hallberg, T.L.I. Jonsson andP.G. Jönsson. A New Approach to Using Modelling for On-line Prediction of Sulfur and Hydrogen Removal during Ladle Refining. ISIJ International, Vol. 44 (2004), pp. 1318-1327.
56. M. Hallberg, L.T.I. Jonsson, P.G. Jönsson and P. Undvall. Sulfur and Hydrogen Refining during Vacuum Degassing—A New Concept for Process Control. Stahl ind Eisen, Vol. 125 (2005), pp. 39-46.

57. K. Harashima, S. Mizoguchi, H. Kajioka and K. Sakakura. Kinetics of Nitrogen Desorption from Liquid iron with Low Nitrogen Content under Reduced Pressure. The Iron and Steel Institute of Japan, Vol. 73 (1987), pp. 1559-1565.
58. K. Harashima, S. Mizoguchi and A. Kiyose. Rates of Nitrogen and Carbon Removal from Liquid Iron in Low Content Region under Reduced Pressures. ISIJ International, Vol. 32 (1992), pp. 111-119.
59. N. Bannenberg, B. Bergmann and H. Gaye. Combined Decrease of Sulfur, Nitrogen, Hydrogen and Total Oxygen in Only One Secondary Steelmaking Operation. Steel Research, Vol. 63 (1992), pp. 431-437.
60. P. Jönsson and L. Jonsson. The Use of Fundamental Process Models in Studying Ladle Refining Operations. ISIJ International, Vol. 41 (2001), pp. 1289-1302.
61. R. Higbie. The Rate of Absorption of a Pure Gas into a Still Liquid during Short Periods of Exposure. Transactions of the American Institute of Chemical Engineers, Vol. 31 (1935), pp. 365-389.
62. S. Alves, J. Vasconcelos and S. Orvalho. Mass Transfer to Clean Bubbles at Low Turbulent Energy Dissipation. Chemical Engineering Science, Vol. 61 (2006), pp. 1334-1337.
63. J. Lamont and D. Scott. An Eddy Cell Model of Mass Transfer into the Surface of a Turbulent Liquid. AIChE Journal, Vol. 16 (1970), pp. 513-519.
64. Prasher and G. Wills. Mass Transfer in an Agitated Vessel. Industrial & Engineering Chemistry Process Design and Development, Vol. 12 (1973), pp. 351-354.
65. R.D. Pehlke and J.F. Elliott. Solubility of Nitrogen in Liquid Iron Alloys II. Kinetics. Transactions of the Metallurgical Society of AIME, Vol. 227 (1963), pp. 844-855.
66. R.J. Fruehan and L.J. Martonik. The Rate of Absorption of Nitrogen into Liquid Iron containing Oxygen and Sulfur. Metallurgical Transactions B, Vol. 11 (1980), pp. 615-621.
67. K. Ito, K. Amano and H. Sakao. Kinetic Study on Nitrogen Absorption and Desorption of Molten Iron. Transactions of the Iron and Steel Institute of Japan, Vol. (28), pp. 41-48.
68. J. Fu, S. Zhou, P. Wang, L. Di and J. ZHU. Effect of Temperature and [S] on the Kinetics of Nitrogen Removal from Liquid Steel. Journal of Materials Science and Technology, Vol. 7 (2001), pp. 233-236.
69. T. Kitamura, K. Miyamoto, R. Tsujino, S. Mizoguchi and K. Kato. Mathematical Model for Nitrogen Desorption and Decarburization Reaction in Vacuum Degasser. ISIJ International, Vol. 36 (1996), pp. 395-401.
70. T. Choh, T. Moritani and M. Inouye. Kinetics of Nitrogen Desorption of Liquid Iron, Liquid Fe-Mn and Fe-Cu alloys under Reduced Pressures. Tetsu-to-Hagane, Vol. (64), 1978, pp. 701-710.
71. H. Ono, K. Iuchi, K. Morita and N. Sano. Effects of Oxygen and Nitrogen on the Rate of Nitrogen Dissolution in Iron-Chromium and Iron-Vanadium Alloys. ISIJ International, Vol. 36 (1996), pp. 1245-1249.
72. K. Morita, T. Hirosumi and N. Sano. Effects of Aluminum, Silicon, and Boron on the Dissolution Rate of Nitrogen into Molten Iron. Metallurgical Transactions B, Vol. 31 (2000), pp. 899-903.
73. H. Ono-Nakazato, T. Koyama and T. Usui. Effect of Surface Concentration of Alloying Elements on Nitrogen Dissolution Rate in Molten iron Alloys. ISIJ International, Vol. 43 (2003), pp. 298-303.
74. C.H.P. Lupis and J.F. Elliott. Generalized Interaction Coefficients: Part I: Definitions. Acta Metallurgica, Vol. 14 (1966), pp. 529-538.

75. D.R. Gaskell. Introduction of Metallurgical Thermodynamic. Scripta Publishing Company, Washington, D.C., (1973).
76. J. Miettinen. IAD - Thermodynamic database for iron alloys. Casim Consulting Oy, Espoo, Finland, (2012).

Aalto-DD 131/2014

ISBN 978-952-60-5838-2
ISBN 978-952-60-5839-9 (pdf)
ISSN-L 1799-4934
ISSN 1799-4934
ISSN 1799-4942 (pdf)

Aalto University
School of Chemical Technology
Department of Materials Science and Engineering
www.aalto.fi

BUSINESS + ECONOMY

ART + DESIGN + ARCHITECTURE

SCIENCE + TECHNOLOGY

CROSSOVER

DOCTORAL DISSERTATIONS